Multi-parametric magnetic resonance imaging for radiotherapy simulation

Tian Li[1], Jihong Wang[2], Yingli Yang[3], Carri K. Glide-Hurst[4], Ning Wen[5], Jing Cai[1]

1 - Department of Health Technology and Informatics, The Hong Kong Polytechnic University, Hong Kong, China
2 - Department of Radiation Physics, Division of Radiation Oncology, MD Anderson Cancer Center, Houston, TX, USA
3 - Department of Radiation Oncology, University of California, Los Angeles (UCLA), Los Angeles, CA, USA
4 - Department of Radiation Oncology, University of Wisconsin, Madison, WI, USA
5 - Department of Radiation Oncology, Henry Ford Health Systems, Detroit, MI, USA

Corresponding Author:

Jing CAI, Ph.D

Department of Health Technology and Informatics

The Hong Kong Polytechnic University

Hong Kong, China

Email: jing.cai@polyu.edu.hk

Running Title: mpMRI for RT simulation

Key Words: Multi-parametric MRI, mpMRI, MRI-guided radiotherapy, MRI Simulation, MRI-linac, machine learning, artificial intelligence

Abstract

Magnetic resonance imaging (MRI) has become an important imaging modality in the field of radiotherapy (RT) in the past decade, especially with the development of various novel MRI and image-guidance techniques. In this review article, we will describe recent developments and discuss the applications of multi-parametric MRI (mpMRI) in RT simulation. In this review, mpMRI refers to a general and loose definition which includes various multi-contrast MRI techniques. Specifically, we will focus on the implementation, challenges and future directions of mpMRI techniques for RT simulation.

1 Introduction

In the last decade, the utilization of magnetic resonance imaging (MRI) in the field of radiotherapy (RT) has seen a steady but definitive increase, ranging from MRI simulation and treatment planning to treatment assessment and integrated MRI-guided RT systems (e.g. MR-linac from ViewRay and Elekta).[1-3] Tethered to changes in RT practice, the utilization of quantitative (e.g. diffusion-weighted imaging [DWI]) to assess intra-treatment responses and to predict outcomes has also seen a dramatic increase in research activity.[4-7] Recent advances in MRI include a new type of imaging acquisition sequence in which multiple image sets (e.g. T_1 and T_2) can be obtained with a single acquisition.[8-11] In this review, multi-parametric MRI (mpMRI) techniques refers to a general and loose definition which includes various multi-contrast MRI techniques. These imaging approaches provide information on certain biological characteristics of bodily tissues, which may be indicative of normal or pathological changes.[12-14] These multi-parametric images, when analyzed together, are hypothesized to reveal fundamental biological changes during

therapy and can predict treatment outcomes and toxicity. This has become an active area of research in the field of RT.[15-18]

In response to the generation of mpMRI images, another area of active research is the use of various techniques to acquire and analyze mpMRI images more efficiently, such as the use of machine learning (ML) and artificial intelligence (AI).[19-22] Compressed sensing and ML are becoming widely applied for faster image acquisition and to improve image quality, even with sparse acquisition in the k-space.[23-26]

This review article will discuss the implementation and challenges of mpMRI in the RT simulation and provide insights into some of the emerging applications in this domain.

2 RT simulation

2.1 Simulation process

The application of MRI in the field of RT often starts with MRI acquisition for RT simulation.[27] Like computed tomography (CT) simulation, the purpose of MRI simulation is to obtain patient images, preferably in the treatment position. However, unlike CT, MRI has superb soft tissue contrast, which enables more accurate and confident target delineation and contouring.[28] Multi-parametric imaging may be performed to obtain a baseline (or pre-treatment time point +imaging), which can be used as additional information for margin determination and dose spatial re-distribution and compared with subsequent imaging to identify treatment-associated changes.[29-31]

Currently, many radiation oncology departments do not have dedicated MR simulators; thus, MRI scanners must be shared with radiology departments, which is suboptimal because imaging for RT planning often requires patients to be imaged in certain immobilization devices

(e.g. VacLok).[32] Nevertheless, MRI and third-party vendors have supplemented diagnostic MRI devices with peripheral devices (e.g. coil holders to accommodate immobilization devices, external lasers, and flat table tops) to make MRI simulation scans more comparable to CT simulation.[33] We expect that dedicated MR simulators will become commercially available in the coming years.

Typically, RT simulation scans are performed with patients in motion-restraining or immobilization devices. Currently, the MRI scanner couch is overlaid with a flat board with index notches that allow for lock-down of VacLok and other patient-positioning devices.[34] Additionally, scans are often performed with surface coils overlaid on a coil holder, such that the weight of the coils will not change the outer contour of the body. Typically, conventional head and neck coils are not used for diagnostic scans because patients are usually scanned with facemasks, which do not fit conventional head and neck coils; thus, a set of surface coils are often used to provide coverage as well as to accommodate the mask.[35-37]

Once the scans are completed, images are transferred to the treatment planning system and are often fused with CT simulation images from which electron density information can be obtained.[38] However, an MR-only workflow has been developed in which electron density information can be obtained by MRI using a technique called synthetic CT.[39-41] This negates the CT simulation scan, which in turn simplifies the simulation and treatment planning process.

2.2 Imaging requirements

Compared with diagnostic MRI, RT simulation using MRI typically has a more limited number of sequences than with diagnostic scans. In addition, RT simulation has the following specific requirements: (1) patients must be scanned in immobilization devices; (2) imaging slice

thickness is typically thinner in RT simulation scans; (3) imaging scans for RT are typically performed in the axial plane, unlike diagnostic scans in which scans are oblique (e.g. spinal scans); and (4) patient positioning, physiological status (respiratory state, bladder filling, etc.), and scanning range are matched for RT purposes, while for diagnostic scans, these requirements are often ignored or not strictly enforced.[33] Otherwise, the processes of patient safety screening, intravenous contrast administration screening, and scanning are rather similar.

3 Multi-parametric MRI techniques

One of the major strengths of MRI is its versatility in visualizing tissue contrast. By activating various contrast mechanisms in MR pulse sequences, mpMRI allows visualization and assessment of tissues based on a range of intrinsic physical and physiological properties, including their T_1 and T_2 values, magnetic susceptibility, blood perfusion, blood vessel permeability, cellular density, and oxygenation.

3.1 Weighted images

The earliest and most widely used tissue contrast mechanisms are T_1- and T_2-weighted qualitative imaging techniques. These weighted images have been implemented in most of the MRI protocols and have been used to provide anatomical information in RT simulation. With these techniques, tissue contrast originates from differences in T_1 and T_2 values between tissues, and the echo time (TE) and repetition time (TR) are tuned to provide the desired tissue contrast. For example, a T_1-weighted (T_1w) image are typically produced by using short TE and TR, while a T_2-weighted (T_2w) image uses long TR and TE. The specific applications of the weighted MRI depend on the disease sites. For example, the T_1w image can be used to differentiate the

hepatocytes from tumor in liver cancer while the T_2w image can be used to visualize the pancreatic and common bile ducts to help define the tumor extension in pancreatic cancer.[42,43] Apart from the T_1w and T_2w MRI, the T_2*w MRI, in which faster T_2* relaxation time caused by magnetic field inhomogeneity is measured, has been used to probe tissue iron deposition and hemorrhage.[44,45]

3.2 Quantitative images

The T_1/T_2/T_2* contrast mechanism of MRI can be further enhanced using gadolinium (Gd) contrast agents. By shortening the tissue T_1 and T_2 relaxation times, Gd boosts the MRI signal when a T_1w pulse sequence is used. Gd agents typically have a small molecular size and traverse freely across capillary walls.[46] After intravenous administration, Gd agents enhance the tissue signal following blood flow into the tissue of interest, enabling investigators to probe tissue blood perfusion and blood vessel permeability. Pre-contrast images are usually acquired as well to relate the post-contrast images. Such a strategy, named dynamic contrast-enhanced MRI (DCE-MRI), acquires a dynamic series of T_1w images that covers both the initial first passage of the Gd contrast into the tissue (wash-in) and the delayed phases when the Gd is slowly cleared out of the tissue (wash-out). Based on the arterial input function (AIF), which refers to the concentration of tracer in blood-plasma in an artery measured over time, it is possible to qualitatively assess tissue perfusion and to calculate several semi-qualitative parameters as surrogates for tissue perfusion, such as the slope of the initial wash-in curve and the area under the curve.[47] Moreover, it has been shown that sophisticated multi-compartmental models can be used to extract quantitative parameters based on the same temporal signal enhancement curves.[48] The most commonly derived parameters include K^{trans} (the volume transfer constant of Gd from the intravascular space to the extracellular extravascular space [EES]), K_{ep} (the volume transfer constant of Gd from the EES to

the intravascular space), and V_e (the fractional volume of the EES). Due to its ability to probe the physiology of the tumor microenvironment, DCE-MRI has shown great potential as a method to evaluate and predict the tumor response to RT and chemotherapy.[49-51] Apart from the DCE-MRI, dynamic susceptibility contrast (DSC) MRI is one of the most frequently used techniques for perfusion measurement, which relies on the Gd-based contrast agent (GBCA) related susceptibility induced signal loss on T_2*w imaging. It is a common technique used for the glioblastoma patients and has demonstrated the ability for differentiation among tumor recurrence, tumor necrosis, and pseudo progression.[52] However, further development and evaluation should be conducted to explore the full potential of DSC-MRI in RT.

Both DCE-MRI and DCS-MRI require Gd contrast, which may represent a disadvantage when imaging needs to be performed repeatedly to longitudinally monitor the tumor response to RT as studies have shown that GBCAs have potential toxicity effects, such as allergic reactions, nephrotoxicity, and even fatal nephrogenic systemic fibrosis.[53-55] Its signal depends on the blood perfusion, which is a more indirect measure of the response of the tumor. DWI, as a quantitative imaging modality, does not require an exogenous contrast agent and has widespread applications in RT diagnosis and prognosis.[56-58]

With DWI, images are acquired by measuring the random Brownian motion of water molecules within a tissue voxel.[59,60] Restricted diffusion appears bright on DWI, whereas free diffusion corresponds to a dark signal. Apparent diffusion coefficients (ADCs) can be calculated from isotropic images obtained by DWI or by calculating the arithmetic mean of the ADCs generated from each directional diffusion map. The diffusion is “apparent” because water movement in the body is affected by the cellular environment and human conditions. The degree of diffusion weighting in an image is controlled by the b-value. The higher the b-value, the more

pronounced the diffusion-related signal attenuation. As the diffusivity of water molecules in the extracellular environment is generally larger than in the intracellular environment, the diffusion MRI signal is very sensitive to cellularity. Tumors with cell death in response to RT generally have a reduced cellular density and hence a high ADC.[61] Therefore, DWI is suitable for monitoring the response of the tumor to therapy. The optimal timing of DWI for the maximal treatment response assessment has to be determined based on the type of tumors and treatment strategies.[62] For example, a study has demonstrated that significant ADC change has been observed at week 6 during fractionated RT course for prostate cancer[63], while another study has demonstrated that the ADC values for cervical cancers increased robustly after 2 weeks of chemo-RT[64].

In the era of precision medicine, it is highly desirable to predict the tumor's response early in the course of therapy so that adjustments can be made to address non-responding tumors. Early results have shown that DWI, either acquired intermittently during therapy or longitudinally at regular time intervals, has the potential to provide accurate information about the tumor response to therapy.[65-67] These data may be incorporated into future prospective adaptive RT trials.

In the context of tumor physiology, oxygenation is of central importance. The degree of tumor oxygenation has a direct impact on the radioresistance of tumor cells.[68-70] Oxygenation MRI could therefore prove highly impactful in the assessment of the tumor response. In particular, blood oxygenation level-dependent (BOLD)-MRI detects differences in oxygenated and deoxygenated hemoglobin. Deoxygenated hemoglobin is paramagnetic, whereas oxygenated hemoglobin is not. As a result, deoxygenated hemoglobin causes local proton dephasing, shortens T_2*, and reduces the signal from tissues in the immediate vicinity. Using BOLD-MRI sequences with T_2*w imaging, the degree of tissue oxygenation can be inferred without the use of an exogeneous contrast agent. Currently, BOLD-MRI still suffers from a low signal-to-noise ratio (SNR) and confounding factors,

such as static magnetic field (B_0) inhomogeneity. Oxygen Enhanced MRI (OE-MRI) is another technique that detect the spin-lattice relaxation rate contrast which is directly related to the concentration of free oxygen molecules.[71] Therefore, the OE-MRI can also provide information related to hypoxia and has been investigated for RT response recently.[72,73] Further developments and optimizations may lead to promising non-invasive means for detecting and monitoring tumor hypoxia.

4 Implementation

4.1 Benchmarking and quality assurance of mpMRI

At present, benchmarking of quantitative performance metrics in MRI has been largely established by the Quantitative Imaging Biomarker Alliance working groups. Through the development of consensus profiles[74] to standardize imaging methods, several mpMRI approaches, including DWI, DCE-MRI, and DSC-MRI, have been determined as sufficiently reproducible in the established literature. One commonly used benchmarking endpoint is repeatability, which is a measure of precision based on replicate measurements taken over a short period of time. Repeatability assessment requires fixed parameters and a fixed scanner, operator, and reconstruction algorithm. A common descriptor is the within-subject coefficient of variation in a test/retest design.[74] Reproducibility also involves replicate measurements over a short period of time, but in this case, a procedural aspect is varied, such as the timing, operator, or MRI platform. Reproducibility is defined by the least significant difference between two repeated measures under different conditions. DWI-specific quantitative performance metrics also include ADC bias at the magnet isocenter, random error within a region of interest (e.g. precision), SNR at each b-value, dependence of the ADC on the b-value, and ADC spatial dependence.

4.1.1 Phantoms for mpMRI benchmarking

Perhaps the simplest phantom for quantitative MRI benchmarking is one that consists of a tube filled with distilled water surrounded by ice water at 0°C, which is known to have a standard diffusion coefficient of 1.10×10^{-3} mm^2/s.[75] For evaluation over a larger range of expected values, another diffusion phantom (High Precision Devices Inc., Boulder, Colorado) containing 13 vials of aqueous solution of 0%–50% w/w polyvinylpyrrolidone surrounded by ice water to ensure measurements at 0°C may also be used.

At present, several phantoms have demonstrated the utility for multi-institutional quantitative MRI benchmarking. One such example is the National Institute of Standards and Technology (NIST) traceable NIST/ISMRM System Standard Phantom[76,77] (QalibreMD, Boulder, Colorado), which consists of multiple layers with embedded sphere vials that span value ranges for quantitative T_1, T_2, and proton density (PD) mapping using varied nickel chloride ($NiCl_2$), manganese chloride ($MnCl_2$), and water concentrations, respectively. Similarly, the Eurospin TO5 phantom (Diagnostic Sonar, Livingston, Scotland) contains doped gel-filled tubes to evaluate T_1 and T_2 mapping and tubes that can be used to vary the concentration of Gd contrast agent for benchmarking. These phantoms have been implemented to benchmark mpMRI sequences in diagnostic MRI,[76-80] low-field MR-linacs,[81] and high-field MR-linacs.[82]

Recently, a novel quantitative MRI phantom has been introduced that leverages three-dimensional (3D) printing to create anatomy-mimicking slabs containing gels doped with different concentrations of $NiCl_2$ and $MnCl_2$ to yield T_1 and T_2 values, respectively. The initial results appear promising to within ~10% of expected with realistic human geometries.[83] Regardless of the phantom used, mpMRI endpoints have a temperature dependence[84,85]; thus, experimental designs

should ensure that phantoms equilibrate to room temperature (or to the temperature required for quantification) and undergo temperature monitoring.

4.1.2 Quantitative accuracy

Several investigator-led multi-institutional comparisons have been made to help establish confidence intervals and benchmarking data for mpMRI sequences, as outlined in **Table 1**. These data can also be developed by adding technical assessment procedures based on a specific clinical trial protocol to yield tighter confidence limits for quantitative metrics.

Table 1: Multicenter benchmarking studies and key results for mpMRI.

mpMRI sequence	#Institutions/MRI scans/field strengths	Phantom	Key methods	Key results
DWI[86]	18/35/1.5, 3.0 T	Ice water, temperature-controlled diffusion phantom	Uniform protocol, central processing	SD of bore-center ADC of <2%; repeatability of <4.5%. ADC at magnet center: intra-exam repeatability of <1% Inter-site reproducibility of <3% ADC bias of 5%–15% for off-center measurement due to gradient non-linearity

DWI[87]	26/35/1, 1.5, 3.0 T	Cylindrical doped water phantom	Evaluated b-values of 0–1000 s/mm^2 and 0–3000 s/mm^2	>80% of mean ADCs were <5% from the nominal value Short-term repeatability of ADC of <2.5% for all scanners
T_1/T_2 mapping, DWI, DCE[80]	15/15/1.5, 3.0 T	ISMRM/NIST phantom DWI phantom	Uniform protocol, central processing Short-term repeatability over three scans DWI data analyzed with the QIBAPhan software package	ADC: -0.007 to 0.029 × 10^{-3} mm^2/s (median repeatability = 3%; reproducibility = 18%) T1: 0.39–1.29 (median repeatability = 1%; reproducibility = 33%) T2: bias = 0.88–0.98 (median repeatability = 1%; reproducibility = 12%) DCE: non-linear vendor-specific relationship between measured and expected with magnitude data, linear with phase data

				Repeatability
T_1 mapping[88]	8/8/1.5, 3.0 T	ISMRM/NIST phantom	Uniform VFA and IR-SE protocols, central processing Repeatability assessed using general linear mixed models Interplatform reproducibility assessed via CoV	VFA: median error = 0.7%–25.8% IR-SE: Median error = 0.2%–8.3% Interplatform reproducibility with VFA was lower at 3.0 T than at 1.5 T and lower than with the IR-SE protocol
T_1/T_2 mapping with MRF[89]	3/4/1.5, 3.0 T	ISMRM/NIST phantom	Uniform protocol Thirty datasets acquired over 30 days Repeatability and reproducibility	MRF highly repeatable (within-case CoV <4% for T_1 and <7% for T_2) and reproducible (within-case CoV <5% for both T_1 and T_2)

	characterized by
	within-case CoV
	Bias assessed

CoV, coefficient of variation; VFA, variable flip angle; SD, standard deviation; MRF, magnetic resonance fingerprinting; IR-SE, inversion recovery spin echo.

4.1.3 Geometric accuracy

High geometric fidelity is of paramount importance in MRI for RT. The accuracy of spatial mapping depends upon several factors, including field uniformity and the linearity of a particular magnet's gradient system, which is the major contributing factor. Imperfection in these parameters results in geometric distortion. While MRI vendors incorporate two-dimensional (2D) and 3D correction algorithms to correct raw MRI data for known gradient non-linearities (GNLs) in their gradient coil designs, residual distortion still exists in the images, particularly as the distance from the magnet isocenter increases.[90-93] As a result, efforts should be made to center the prescribed imaging volume near to the center of the magnet bore to reduce the impact of GNL. For example, in an evaluation of 35 clinical MR systems performed at 18 institutions with a uniform data acquisition protocol and phantom coupled with central processing, large ADC non-uniformity errors (5%–15% bias) were present for off-center measurements (±110 mm in the right-to-left [R/L] direction and ±70 mm in the superior-to-inferior [S/I] direction) that were consistent with GNL.[86] Recent guidance from AAPM TG-284 suggests that due to the stability of GNL, it should be characterized during commissioning and after major equipment changes.[33] Another critical

parameter that impacts the geometric distortion is the slew rate of the magnet as it impacts the readout bandwidth. Stronger gradients and faster slew rates will shorten effective echo times and subsequently reduce geometric distortion in echo planar imaging (EPI)-based DWI and other quantitative imaging applications. Large-volume phantom, such as the GRADE phantom from Spectronic Medical AB, 604-GS phantom from CIRS, and GrID phantom from Gamma Gurus, can be used to evaluate the geometric distortion of the large-bore MRI in RT applications.[94]

4.2 Application of mpMRI

Many patients who require RT will undergo an mpMRI scan to facilitate tumor delineation or subvolume targeting. However, potential pitfalls may occur if mpMRI is used without discrimination and caution. In this section, the practical aspects of implementing and interpreting mpMRI will be discussed.

4.2.1 Site considerations

The applications of mpMRI at different disease sites have different requirements and considerations. However, one shared practice for different sites is that mpMRI should ideally be acquired with an immobilization device in the treatment position. This reduces deformation, registration error between MRI and planning CT, and motion artifacts, which in turn improves the registration efficiency, image quality, and contour accuracy. The typical mpMRI sequences used in RT for different sites are summarized in **Table 2**. Common practice for different sites is discussed in the following sub-sections.

Table 2: Typical mpMRI sequences used in RT for different sites.

		T_1w	**T_2w**	**DWI**	**Cine**	**FLAIR**
Brain	Acquisition	3D	2D axial	2D axial	NA	2D axial
	Contrast agent	Pre-/post-contrast	Pre-/post-contrast	Pre-contrast	NA	Pre-/post-contrast
Head and neck	Acquisition	2D axial	2D axial	NA	NA	NA
	Contrast agent	Pre- and post-contrast	Pre-contrast	NA	NA	NA
Lung	Acquisition	3D	2D axial	2D axial	2D in three directions	NA
	Contrast agent	Pre-/post-contrast	Pre-contrast	Pre-contrast	Pre-/post-contrast	NA
Breast	Acquisition	2D axial/3D	2D axial and sagittal	NA	NA	NA
	Contrast agent	Pre-/post-contrast	Pre-/post-contrast	NA	NA	NA
Abdomen	Acquisition	2D axial/3D	2D axial	2D axial	2D in 3 directions	NA
	Contrast agent	Pre-/post-contrast	Pre-contrast	Pre-contrast	Pre-/post-contrast	NA
Pelvis	Acquisition	2D axial/3D	2D axial and sagittal	2D axial	NA	NA

Contrast agent	Pre-/post-contrast	Pre-/post-contrast	Pre-contrast	NA	NA

4.2.1.1 Brain

With brain MRI, the most popular T_1w sequence is inversion-recovery gradient echo (IR-GRE). Turbo spin-echo (TSE) is most commonly used for T_2w imaging and fluid-attenuated inversion recovery (FLAIR) imaging, and EPI is most often used for DWI. **Figure 1** demonstrates an example of mpMRI images from a patient with brain cancer. The in-plane resolution requirement for T_1w, T_2w, FLAIR, and post-contrast T_1w imaging is typically 1 mm isotropic and less than 2 mm isotropic for DWI. The primary concern of MRI simulation of the brain is the accuracy of tumor depiction, especially in the context of stereotactic radiosurgery.[95] Ideally, isotropic 3D sequences are preferred for this purpose because they are resistant to partial volume effects, are less affected by B_0 inhomogeneity, and are continuous without gaps. Three-dimensional IR-GRE sequences are widely used for brain tumors and are suggested by the standardized brain tumor imaging protocol.[96] However, 3D TSE and 3D gradient echo with volume interpolated sequences (VIBE by Siemens, LAVA-Flex by GE, THRIVE by Philips, 3D Quick by Canon, and TIGRE by Hitachi) are also frequently used for brain MRI simulation. Studies have also shown superior tumor contrast and neuroradiologist rating for 3D TSE sequences compared with 3D IR-GRE and 3D gradient echo with volume interpolated sequences.[97-100] However, 3D sequences may not be available for all sequences and scanners. In such cases, a slice thickness of less than 4 mm is recommended with no gap on 1.5-T scanners and less than 3 mm with no gap on 3.0-T scanners. DWI is typically acquired with b-values of 0, 500, and 1000 s/mm^2 on both 1.5-T and 3.0-T scanners. Post-contrast T_2w imaging is typically used for its hyperintense tumor

appearance to aid tumor visualization. FLAIR imaging is used for suppression of the fluid signal to increase tumor conspicuity. It is worth noting that FLAIR imaging has a lower SNR intrinsically than other standard sequences. Therefore, an 8-16 echo train length is recommended for FLAIR imaging. Contrast injection is usually conducted after T_1w imaging, FLAIR imaging, and DWI. Post-contrast T_1w imaging is usually performed between 4 and 8 minutes after contrast injection, with T_2w imaging acquired right before T_1w imaging. However, several studies have reported better tumor visualization 15–20 minutes after contrast injection.[101,102] Also, a higher dose of contrast agent has also been proven as helpful for tumor visualization.[103] Therefore, the specific protocol should be determined based on the condition of the patient, the hardware, and the clinic workload, amongst other considerations.

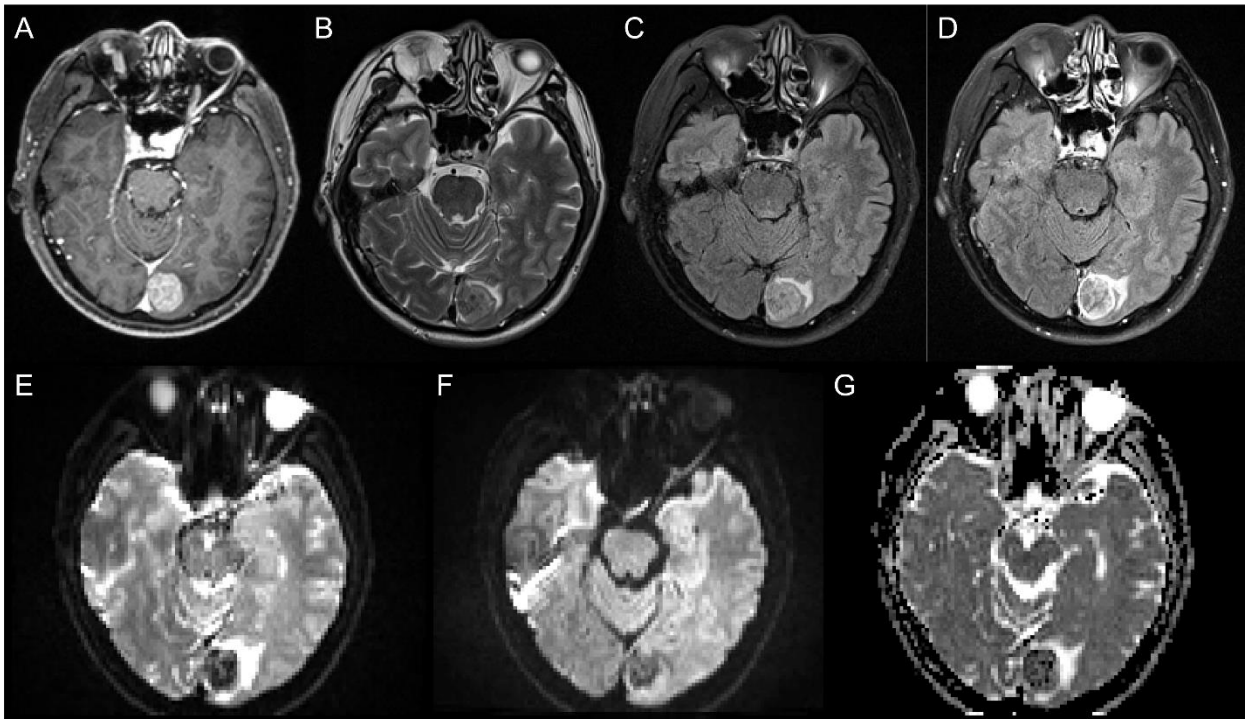

Figure 1. Example mpMRI images from a patient with brain cancer. A shows the 3D post-contrast T_1w image using fast gradient echo sequence. B shows the 2D axial pre-contrast T_2w image using TSE. C shows the 2D axial pre-contrast FLAIR image. D shows the 2D axial post-

contrast T_2w image using FLAIR. E and F show the 2D axial pre-contrast DWI images with b-values of 50 and 1000, respectively. G shows the ADC map derived from E and F.

4.2.1.2 Head and neck

Unlike the brain region, the head and neck region requires a larger field of view in superior-inferior direction; thus, 3D sequences are not ideal for application in this region. Two-dimensional sagittal/coronal pre-/post-contrast T_1w/T_2w MR images are occasionally included to minimize the acquisition time, avoid aliasing, and provide a better view of certain anatomy. However, unlike diagnostic MRI, axial images are still mostly used for the purposes of registration and contouring. Fat saturation techniques are frequently used in this region to better visualize the tumor and surrounding organs. Another promising sequence for the head and neck region is DWI. Although it has not been widely accepted as a clinical standard to image the head and neck region, several studies have revealed the ability of DWI to aid early visualization of primary tumors and nodal involvement, and to predict treatment outcomes.[4,104,105] However, its application in the head and neck region is still hampered by large geometric distortion because of the structural complexity of this region.[106] Nevertheless, research is being conducted to solve this problem using dedicated acquisition and post-processing methods. For example, the RESOLVE sequence from Siemens (or MUSE from GE, DWI with segmented EPI from Philips, and FASE DWI from Canon) is a multi-shot EPI technique that could reduce the distortion in DWI in head and neck region.[107] It is conceivable that DWI will be incorporated into clinical protocols for head and neck imaging in more centers in the future.[108,109]

4.2.1.3 Lung

Current lung cancer RT strategies are mostly based on CT, and the application of MRI in the lung is limited because of the low PD of lung tissue, magnetic susceptibility, and respiratory motion.[110] However, MRI can help in tumor delineation and motion management for certain lung cancer cases, including lung cancers located at the mediastinum and at the lung periphery.[111-114] A typical T_2w sequence used for the lung is axial single shot fast spin echo (HASTE by Simens, Single-shot FSE by GE, Single-shot TSE by Philips, FASE by Canon, and single shot FSE by Hitachi) pre-contrast T_2w for its fast speed. Different from the other static body parts, 2D cine images are often needed in lung regions to assess the motion range of the lung tumor. Because of compromised lung function in patients with lung cancer, it is difficult for most patients to hold their breath during MRI. Therefore, free-breathing or gated acquisition schemes are mostly used for patients with lung cancer. One study has shown sufficient image quality for RT purposes using free-breathing StarVIBE and SpiralVIBE sequences, indicating a potential improvement in scanning efficiency.[115]

4.2.1.4 Breast

Whole-breast irradiation is typically administered for 5-7 weeks after lumpectomy. The goal of mpMRI of the breast is therefore mainly focused on the identification of lumpectomy sites and lymph nodes. For example, the T_1w sequence can be used to provide anatomical information and delineate lymph nodes, while the T_2w sequence is typically used for lumpectomy site identification.[43,116-118] When imaging the breast, the mpMRI sequences are typically conducted with fat saturation for better visualization of the target area.

4.2.1.4 Abdomen

Abdominal MRI plays an important role in RT for better tumor visualization. Similar to lung mpMRI, 2D cine images are often used for tumor motion measurement. Fat saturation techniques are used in most abdominal MRI scans to suppress the fat signal in this region. Post-contrast T_1w scans of the abdomen may be acquired in different phases to visualize different targets. For example, arterial-phase contrast-enhanced T_1w imaging may be used for primary cancer, and delayed-phase contrast-enhanced T_1w imaging may be used for hypo-vascular metastases.[43] It is critical to ensure the repeatability of positioning in simulation and RT treatment for abdominal cancers, especially for gastric cancer [119]. One possible practice is to ask patients to drink a certain volume of water (e.g. 500 mL) before abdominal MRI and RT treatment [120].

4.2.1.5 Pelvis

Typical cancers in the pelvic region include prostate, rectum, and cervical cancer. The mpMRI sequences for these cancers include 2D axial pre-contrast T_2w, 2D sagittal pre-contrast T_2w, 2D axial/3D pre-contrast T_1w, 2D axial pre-contrast DWI, and 2D axial/3D post-contrast T_1w sequences. Fat saturation is also commonly used in this region to improve visualization of different organs. T_2w imaging is typically used for organ delineation, including the prostate, rectum, and bladder.[43,121,122] Similar to abdominal MRI scanning practice, water consumption (e.g. 300 mL) before scanning is recommended to increase the positioning repeatability, especially for prostate cancer MRI scanning[123-127].

4.2.2 Respiratory motion management

Respiratory motion is the most prevalent motion for thoracic and abdominal tumors and has been investigated intensively over the years.[128-133] Organ motion may also compromise the

image quality of different mpMRI sequences. For example, DWI is sensitive to the random motion of water molecules and bulk organ movement (e.g. cardiac and respiratory motion). Such motion can degrade the quality of DWI and create artifacts and quantitative errors. The organs and tissues that are prone to respiratory motion include the lungs, esophagus, breast, prostate, kidney, pancreas, and liver. In some studies, researchers have measured the tumor or the host organ, while in other studies, surrogate organs, such as the diaphragm, have been measured. According to different studies, breathing patterns vary in amplitude, rate, and regularity during the whole RT process.[134-137] Large variations between patients have also been demonstrated, indicating the need for personalized respiratory management.[138-140]

The reported motion measurement results for lung tumors vary significantly across different studies. Dinkel *et al.* reported an average lung tumor motion of 7.4 mm in the LR direction, 7.4 mm in the anterior-to-posterior (AP) direction, and 6.6 mm in the SI direction in seven patients with bronchial carcinoma using four-dimensional (4D) MRI.[141] Thomas *et al.* investigated intrafractional lung tumor motion using the ViewRay system and reported that the largest tumor centroid motion (± standard deviation [SD]) was within 18.0 ± 3.0 mm.[142] Respiratory motion not only has a significant influence on lung tumors, but also on abdominal tumors. In general, the SI direction is the dominant direction in which abdominal organ motion occurs, while in the AP and LR directions, the motion amplitude is usually less than 2 mm.[143-145] Akino *et al.* previously investigated liver tumor motion using cine MRI in six patients with stereotactic body radiation therapy (SBRT) and reported an average tumor motion of 2.4 ± 1.4 mm, 4.4 ± 3.3 mm, and 14.7 ± 5.9 mm in the LR, AP, and SI directions, respectively.[144] Yang *et al.* measured pancreatic tumor motion using 4D-MRI in 10 patients undergoing RT and reported a tumor motion of 3.6 ±1.5 mm in the SI direction.[143] Nonaka *et al.* quantified different abdominal organ motions in 35 volunteers

using cine MRI and reported an average kidney motion of 1.0 mm in the LR direction, 1.0 mm in the AP direction, and 2.0 mm in the SI direction.[145] All of these studies have suggested that abdominal cancer can move significantly in the SI direction and that it can vary considerably between patients. Therefore, accurate measurement of tumor motion for each individual is crucial for accurate radiation dose delivery to the target.

4.2.2.1 Motion artifact reduction

Motion-induced artifacts are most commonly seen in the chest and abdominal regions. In RT simulation, immobilization devices can reduce patient motion and ensure reproducibility between the simulation and treatment.[146] In addition to immobilization devices, several techniques have been proposed to reduce artifacts, which can be grouped into three general categories: acquisition acceleration, motion compensation, and AI-assisted approaches. Acquisition acceleration techniques include parallel imaging, compressed sensing, and simultaneous multi-slice excitation.[147-155] These acceleration techniques can be used individually or in combination to improve the acquisition speed and reduce motion artifacts. However, these techniques can compromise the SNR and other artifacts, such as parallel imaging artifacts.[156,157] Motion compensation techniques are widely used in clinical practice, including breath-hold, respiratory synchronization, and non-Cartesian sampling.[158-168] Breath-hold is a straightforward method to obtain a satisfactory image quality. However, breath-hold may limit the total acquisition time and restrict the image resolution due to the limited acquisition time available per breath-hold.[169,170] The repeatability of the breath-hold phase and compromised lung function in certain patients have hampered the use of breath-hold in a large proportion of patients undergoing RT. For these patients, respiratory synchronization techniques may be applied for artifact reduction. Respiratory

synchronization can be achieved by tracking respiratory motion using external or internal surrogates. Three methods are typically used, including triggering, gating, and tracking. However, respiratory synchronization techniques may be challenged by breathing irregularity, uncertainty in respiratory surrogates, and prolonged scanning times. Non-cartesian sampling techniques, such as radial sampling (e.g. StarVIBE, RadialVIBE, and BLADE from Siemens; PROPELLER from GE; RADAR from Hitachi; JET from Canon; and MultiVane XD from Philips) alleviate motion artifacts during acquisition because they are not propagated in the phase-encoding direction due to different k-space line directions. AI-assisted approaches for artifact reduction have also been proposed.[171-176] These approaches remove motion artifacts through reconstruction or post-processing, and they have yielded promising results. However, these methods still need to be verified before clinical application.

4.2.2.2 4D-MRI

Over the last 20 years, various researchers have proposed numerous methods for 4D-MRI, which have yielded promising results in both volunteers and patients.[177] It can provide valuable information for image-guidance of RT including the tumor motion amplitude, tumor localization, treatment verification, and treatment monitoring.[178,179] **Figure 2** demonstrates an example of 4D-MRI in a patient with liver cancer. Several reconstruction methods have been developed for 4D-MRI generation, and they can be grouped into two main categories: 1) prospective 4D-MRI and 2) retrospective 4D-MRI.

Prospective 4D-MRI can be achieved using real-time 3D acquisition or fast 2D acquisition with a respiratory triggering system to preselect respiratory amplitudes.[180-187] Compared with retrospective reconstruction methods, prospective reconstruction methods acquire images in pre-

459 determined conditions, which makes them less susceptible to breathing irregularity. However,
460 preselection of respiratory amplitudes is achieved in the preparation stage before real image
461 acquisition. Thus, if there is a substantial difference in the patient's breathing pattern or baseline
462 between the preparation and acquisition stages, the acquisition time will be prolonged. This
463 phenomenon limits the clinical application of this technology. For example, Yuan *et al.* proposed
464 a 4D-MRI technique that uses the commercial 3D gradient echo with volume interpolated sequence
465 with controlled aliasing in parallel imaging, which results in higher acceleration.[180] However, the
466 relatively low temporal and spatial resolutions (0.615 s/volume and 2.7 × 2.7 × 4.0 mm^3,
467 respectively) and the commonly seen motion artifacts of their method still need further
468 improvement for most RT applications. Du *et al.* developed a prospective amplitude-triggered 4D-
469 MRI protocol that uses respiratory state splitting to improve triggering efficiency.[181] Their 4D-
470 MRI protocol offers a T_2w sequence for better tumor visualization.

471 Retrospective 4D-MRI can be achieved by continuously acquiring images with a
472 respiratory signal recorded simultaneously and then assigning 2D slices to corresponding
473 respiratory phases using internal or external surrogates.[188-196] Many studies have used fast MR
474 sequences, including spoiled gradient echo and balanced steady-state free precession (bSSFP)
475 sequences. For example, Cai *et al.* developed a retrospective 4D-MRI technique that uses an
476 image-based surrogate for respiratory motion.[190] A 2D fast T_2w/T_1w steady-state free precession
477 MR sequence was used in their study, which showed that the proposed 4D-MRI technique can
478 accurately measure respiratory motion in patients with liver cancer with an error of less than 1 mm.
479 However, although fast, spoiled gradient echo and bSSFP sequences are T_1w and T_1w/T_2w,
480 respectively, meaning that they demonstrate insufficient tumor–tissue contrast, even with Gd
481 enhancement. To provide better tumor contrast, Liu *et al.* developed a novel result-driven phase-

sorting method, which selects the most representative image from redundant images in each phase for 4D-MRI with a T_2w HASTE high-speed sequence.[191] Compared with 2D acquisition methods, 3D acquisition methods provide isotropic voxel sizes and higher SNRs. Buerger *et al.* proposed a 3D golden radial phase encoding with 1-D self-navigation 4D-MRI, which achieved a 1.75-mm isotropic voxel size in ~7 minutes.[192] However, because the TR is generally short with 3D acquisition, the image contrast is usually insufficient for RT applications. Also, the image quality may be impaired by undersampling artifacts in patients with irregular breathing, and the prolonged readout time compared with 2D acquisition requires a more sophisticated pulse sequence design and post-processing techniques.

Nevertheless, 4D-MRI still has not been widely accepted in the clinic, though a considerable number of methods have been published in the literature over the last decade. Future work is required to develop custom pulse sequences and reconstruction algorithms and to further evaluate and improve spatial resolution and integrity.

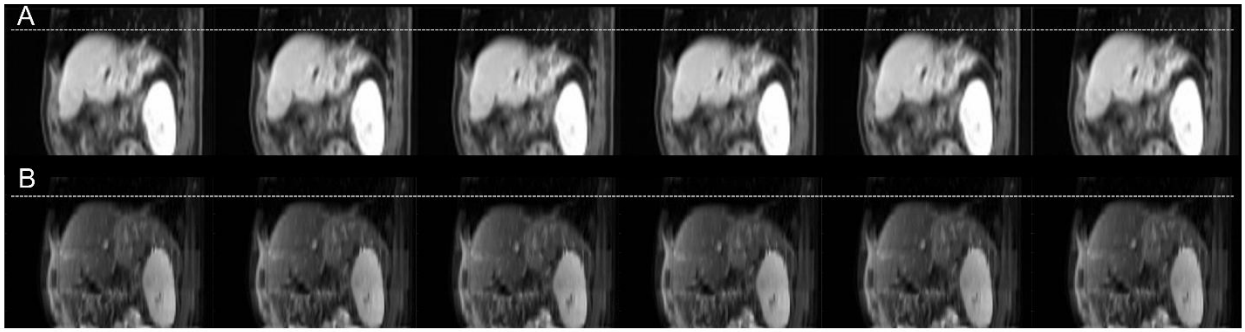

Figure 2. An example of 4D-MRI in a patient with liver cancer. A shows the T_1w 4D-MRI image. B shows the T_2w 4D-MRI image. The white dashed line helps to better visualize motion.

5 Outlook and Discussion

5.1 Challenges to the implementation of mpMRI in the clinical setting of RT

There are still many technical challenges to the implementation of mpMRI for high-precision RT, including the repeatability and reproducibility of quantitative imaging features, management of inter-/intra-fractional motion, improvements in geometrical accuracy and spatial resolution, identification of target boundaries using quantitative imaging parameters, lack of biological validation of the derived parameters, and understanding of complicated quantitative relationships between pathophysiological conditions and imaging features. These challenges have hampered the adaptation of mpMRI in RT simulation and its implementation in further RT applications such as dose escalation, treatment adaptation, and dose painting.

5. 1.1 Challenges with DWI

DWI has a relatively short acquisition time and high contrast resolution between tumors and healthy tissues, which is beneficial for target delineation. However, DWI is sensitive to cell type, geometry, and permeability at the micron scale due to its direct dependence on water diffusion in the tissue microstructural environment. DWI is generally based on single-shot EPI sequences and is highly sensitive to susceptibility errors due to the low-pixel bandwidth in the phase-encoding direction. DWI distortion has contributing factors, including:

- B_0 inhomogeneity
- Applied gradient linearity
- Magnetic susceptibility of the subject, such as an air-filled rectum or endorectal coil balloon and bone–tissue interfaces
- Chemical shift artifacts

- Motion artifacts

The distortions are system-specific, and they also vary from patient to patient. A higher field strength yields a higher SNR, which can be traded off against temporal or spatial resolution to improve contrast. Thus, higher field strengths yield more versatile MRI data and improve image guidance scenarios. However, susceptibility artifacts are increased at higher field strengths and the geometric fidelity is critical in RT simulation. Methods used to correct these distortions typically fall into three categories: retrospective mapping of the magnetic field computed from phase images acquired at different echo times, prospective slice-by-slice shim, and central frequency update,[197] or a combination readout-segmented EPI and parallel imaging by accelerating the k-space traversal in the phase-encoding direction.[198] In the absence of fat-suppression techniques, a high readout gradient can be used to minimize chemical shift artifacts, as well as B_0 and susceptibility effects.

Ultra-high b-value (>1000 sec/mm^2) DWI may improve tumor delineation with highly restricted diffusion from benign tissues and less T_2 shine-through effects.[199,200] However, this comes with the tradeoff of a low SNR, which needs to be compensated by a longer scan time to increase the number of excitations to optimize image quality. In general, a high b-value (>700 sec/mm^2 at 1.5 T and >1000 sec/mm^2 at 3.0 T) is recommended for prostate DWI, and a post-processed ADC map is necessary to identify and evaluate prostate tumors, both objectively and subjectively. Although studies have shown significant differences in ADCs between cancerous and healthy prostatic tissue, ADC values should be interpreted carefully in patient care due to technical variability and lack of consensus on the ADC of cancerous tissue.

The ADC values are derived from a mono-exponential model which contains both diffusion and perfusion information. The intravoxel incoherent motion (IVIM) model can take the perfusion and diffusion parameters into account separately in DWI by using a bi-exponential

function. Generally, the IVIM can describe the DWI signal decay more accurately. Study has shown that the perfusion fraction derived by IVIM is related to the locoregional recurrence after treatment for head and neck patients.[201] However, it also requires higher data quality as it contains four fitting parameters in the bi-exponential model. Other DWI models have also been investigated including the Kurtosis model.[202] However, more investigation is warranted for their validation and application in RT simulation.

5.1.2. Challenges with DCE-MRI

DCE-MRI uses various physiological parameters to quantify tumor perfusion and microvascular vessel wall permeability within tumors and surrounding tissues. It typically takes more than 5 minutes to acquire image sequences due to slow capture of temporal changes in the enhancement of contrast agent passing the capillary wall. There is always a trade-off between the spatial and temporal resolutions for DCE-MRI acquisition, especially for RT simulation where time efficiency is an important consideration. The required spatial and temporal resolutions vary among different body sites. For instance, the acquisition of DCE-MRI for breast, prostate, and liver is more challenging compared to brain and head and neck region. The specific implementation details of DCE-MRI can be found in the QIBA guidelines.[2] The main challenges with DCE-MRI include the reproducibility and technical difficulties in data acquisition, the difficulty in data analysis and interpretation, and model development for quantitative analysis.

Similar to DWI, various approaches have been investigated to address data acquisition to improve the SNR, reduce geometric distortion, increase the readout bandwidth, and apply parallel imaging. DCE-MRI data analysis needs to derive the AIF from the concentration of contrast agent in the blood plasma. Accurate derivation of the AIF is subject to temporal resolution, partial

volume effect, signal non-linearity, and B_1 inhomogeneity.[203] An average cohort AIF derived from a suitable population could achieve better repeatability than individual AIF values.

In the past decade, several models have been utilized for the pharmacokinetic analysis of clinical trial data and animal studies to calculate plasma fraction (v_p), k^{trans}, and v_e.[204-207] However, few studies have examined whether the models are appropriate.[208,209] Model selection using standard statistical practices is almost absent in DCE-MRI studies of vascular physiology; this, in turn, introduces either unnoticed bias (underfitting of data) or excess variance (overfitting), and hinders the extraction of meaningful and reliable information from DCE-MRI studies. Recruiting essential statistical methods and ML models for DCE-MRI data analysis will allow the production of unbiased estimates on tumor permeability parameters. It will also provide additional information regarding the dynamic appearance of different tumor regions. In addition, the reliability of pharmacokinetic maps is subject to the tumor microenvironment. For example, k^{trans} values distinguish between tumor foci and healthy prostatic tissue at the peripheral zone.[210] However, they do not reliably differentiate prostate cancer from benign prostatic hyperplasia within the central zone of the prostate gland due to the similarities in microvascular density exhibited in both conditions.[211]

In addition to the acquisition and imaging processing challenges described above, each imaging modality is acquired with specific settings, and the derived quantitative features also have different indications of lesion characteristics. Therefore, there are challenges to their integration in decision making. Image registration and resampling are needed on a per-voxel basis because each sequence is subject to a different region of interest, voxel size, and distortion. Efforts have been made to understand the correlations among features derived from other modalities and to

interpret them consistently.[212] It is also essential to associate them with histopathological and molecular bases to validate their interpretation for applications in RT simulation.[213-215]

5.2 Potential solutions and future research directions

5.2.1 MR fingerprinting (MRF) and its applications

MRF, which was first proposed by Ma *et al.* in 2013,[8] allows simultaneous quantification of multiple intrinsic tissue properties in a single, time-efficient acquisition. This efficient quantitative property has made MRF appealing to the applications in RT including longitudinal follow-up, multi-center studies, tissue characterization, etc. MRF involves three steps: signal acquisition, pattern matching, and tissue property visualization.[216] During image acquisition, various scanning parameters, including TR, TE, k-space sampling trajectories and flip angle, are varied simultaneously to provide fingerprint-like signal evolution curves. During pattern matching, each voxel's signal evolution curve is retrospectively compared with a dictionary simulated using the Bloch equation[217] to identify the best matching entry. The property associated with the best matching entry is subsequently assigned to the corresponding voxel. It has been demonstrated that the matching process can be achieved successfully even with highly undersampled data, allowing a high acceleration factor to be used in the acquisition process.[218,219] MRF can measure T_1, T_2, B_0, and PD[8] with recent expansions to perfusion,[220] radiofrequency transmit field inhomogeneity (B_1),[221,222] hemodynamic-related properties,[223-225] and T_2*.[226] MRF-derived quantitative maps (T_1, T_2, PD, etc.) have high accuracy and repeatability, with average coefficient of variation values of less than 5% for T_1 and T_2 values[77,89,226-228]

MRF-derived quantitative maps have been investigated for various applications, including diagnosis, tissue characterization, imaging biomarkers, patient follow-up, prognostication, patient

management, therapeutic assessment, and therapy design.[229-233] Currently, the application of MRF focuses largely on the brain,[233-237] including a 3D MRF technique intended for RT applications.[238] For instance, Badve *et al.* used MRF-derived T_1 and T_2 maps to differentiate gliomas and metastases and showed significantly different T_1 and T_2 values.[239] In terms of RT applications, Li *et al.* developed a time-resolved MRF technique for motion management in RT, which has been verified in digital phantoms and volunteers.[240,241]

MRF has shown strong potential for the measurement of multiple tissue properties in a very time efficient acquisition. Assessment of tissue properties and the microvascular environment in one scan can offer significant benefits in RT simulation including time efficiency improvement, protocol standardization, longitudinal assessment, synthetic CT generation, etc. However, there are still discrepancies in various difficult-to-interpret regions, especially for physiological estimations without robust gold-standard references. Continuous development and clinical validation of fingerprints using a combination of MR sequences are still ongoing to make MRF an effective clinical framework.

5.2.2 Rapid non-balanced or bSSFP

In addition to the MRF technique, other novel simultaneous multi-parametric mapping techniques have also been proposed using the mixed T_1 and T_2 sensitivity of rapid multi-echo non-balanced or bSSFP sequences.[10,11,242-245] bSSFP imaging can acquire characteristic tissue-specific frequency profiles to estimate tissue property maps, while non-bSSFP imaging can obtain multiple steady-state configurations for quantitative mapping. Similar to MRF, these multi-parametric mapping techniques can generate quantitative parametric maps in a single scan. The parameters that can be measured with these techniques include T_1, T_2, PD, T_2^*, B_1^+, and B_0. For example,

Heule *et al.* proposed a triple-echo steady state (TESS) relaxometry approach that uses two specific signal ratios among three echoes and a golden section search to generate T_1 and T_2 maps.[244] This TESS method is insensitive to both B_1 and B_0 inhomogeneities, especially for T_2 maps, and has shown reliable T_1 and T_2 measurement results in both phantom and volunteer studies. Heule *et al.* also proposed an artificial neural network fitting method for 3D phase-cycled bSSFP sequences to improve T_1 measurement accuracy.[242] Their method can acquire whole-brain images with an isotropic resolution of 1.3 mm within 11 minutes and satisfactory measurement accuracy. These techniques have been tested mainly in the brain, knee, hip, and wrist for relaxometry.[245-248] Further developments are still warranted, including acceleration and verification, to expand these applications to other body parts and RT applications.

A novel multi-contrast MRI method, namely STrategically Acquired Gradient Echo (STAGE), has also been developed. STAGE produces several quantitative (multi-echo quantitative susceptibility maps [QSM], T1 maps, PD maps, and R2* maps) and qualitative (T1w, enhanced T1w, and PD-weighted) datasets in two image acquisitions,[249-251] enabling reduced acquisition times. The feasibility of STAGE has been demonstrated on a 0.35-T MR-linac in phantoms and in a cohort of patients with brain tumors, in which it showed promise for monitoring the therapeutic response to RT.[81] Upon further verification, this technique may improve the efficiency and help standardize the imaging protocol in RT simulation.

5.2.3 Other potential MR techniques

There are various other mpMRI techniques that have been demonstrated promising for RT applications, such as Amide Proton Transfer (APT) imaging, hyperpolarized MRI, arterial spin labeling (ASL) perfusion imaging, etc. APT imaging is the most studied Chemical Exchange

Saturation Technique (CEST). It utilizes selective off-resonance saturation pulses at 3.5 ppm downfield from the water resonance to detect the amide group of mobile proteins and peptides. The APT effect is usually assessed using the magnetization transfer ratio (MTR) asymmetry analysis at an offset of 3.5ppm, therefore hyperintensity signals on the APTw images associate with increased amide protein content and/or increased amide proton exchange rate.[252] The APT has potentials in imaging malignant tumors with high cellularity that may exhibit elevated amide proteins and peptides.[253] For example, head and neck studies showed higher mean APTw signal in the malignant tumors than the benign tumors[254], and the responder patients to the RT and/or chemotherapy showed more intra-treatment APTw signal change at 2-weeks from pre-treatment.[255] Hyperpolarized MRI is a unique MR technique that probes various functions (perfusion, ventilation, metabolism, etc.) using inhaled or injected hyperpolarized contrast media such as Helium-3, Xenon-129, Carbo-13. For example, hyperbolized Carbon-13 MRI has been shown the potential to predict tumor response by probing lactate metabolism in vivo.[256] Hyperbolized Helium-3 and Xenon-129 MRI have been used to image lung biomechanics and functions which can be used to guided lung cancer RT treatment planning for preserving highly functional lung regions and reducing lung toxicity.[257-260] ASL perfusion imaging uses the labeled blood as the endogenous tracer to quantify cerebral blood perfusion non-invasively. It has been applied to differentiate recurrent gliomas and radiation necrosis.[261] While these emerging techniques have demonstrated their potentials in RT applications, further investigations are warranted to bring them to routine RT clinical practice.

5.2.4 Deep learning (DL) frameworks and their role in image reconstruction and synthesis

683 DL is an AI technique that uses multiple layers to progressively extract higher-level
684 features from the raw input. DL has been implemented to various aspect of mpMRI recently. Raw
685 MR data have been acquired in the k-space using a fully sampled or undersampled approach with
686 parallel imaging or compressed sensing.[25] DL has been incorporated into MR reconstruction with
687 different types of undersampling scheme. The Cascade-Net and its transformations, such as KIKI-
688 Net, have been proposed to de-alias iteratively using a cascade of convolutional neural networks
689 (CNNs) for image reconstruction to reduce overfitting.[262,263] A hybrid cascaded model has been
690 proposed to operate in both the image and k-space domains.[264] With this approach, a complex-
691 valued residual U-net in the k-space domain and a real-valued U-net in the image domain are
692 connected through the magnitude of inverse discrete Fourier transformation. The hybrid approach
693 further improves reconstruction compared with the models that use image domain data only. Yang
694 *et al.* proposed deep de-aliasing generative adversarial network (GAN)-based compress sensing
695 reconstruction.[265] The architecture implements a U-net based generator and a discriminator with
696 standard CNN architecture. The loss function includes the adversarial loss, pixel-wise mean square
697 error loss, frequency domain loss, and perceptual loss derived from the visual geometry group to
698 improve the reconstructed image quality. DL can also be applied to MRF by developing a complex-
699 valued neural network, which can better consider both real and imaginary components of MR
700 signals and map MR signals to tissue properties.[266] As images can be rapidly reconstructed, this
701 approach is suitable for real-time processing, which has great potential in the application of
702 mpMRI for tumor tracking and adaptive RT.

703 Synthetic CT (sCT) generation has been investigated intensively recently especially with
704 the introduction of MR-linac and several methods have been proposed with promising restuls.[267]
705 Among different methods, DL-based sCT generation has been investigated extensively in recent

year and comparisons of using single or multiple MRI sequence as input has been made.[267-271] For example, Tie *et al.* proposed a conditional GAN for sCT using both single and multiple MRI sequence.[271] They reported an increased peak signal-to-noise ratio for multi-sequence training compared to single sequence training.

Recently, an increasing number of DL-based studies have achieved great success in medical image synthesis,[272-276] indicating the possibility of predicting a target MR image from existing MR datasets according to the number of input MR modalities and networks. For example, Yu *et al.* proposed a 3D conditional generative adversarial network to synthesize FLAIR images from its T_1w counterpart to improve brain tumor segmentation performance.[277] Kleesiek *et al.* also developed a 3D Bayesian DL network that uses multi-parametric brain MR modalities, including T_1w imaging, T_2w imaging, FLAIR imaging, DWI, and susceptibility-weighted imaging, to synthesize VCE-T_1w MR images.[272] **Figure 3** shows an example of virtual contrast-enhanced (VCE) MRI in a patient with head and neck cancer.[278]

DL has exhibited superior performance in terms of undersampled data reconstruction, image quality enhancement, synthetic CT generation, and image contrast transformation. Although the accuracy, fidelity, and generalizability of these techniques still need to be verified before clinical implementation, DL hold great promise in improving the time efficiency, image quality, and patient's safety in RT simulation.

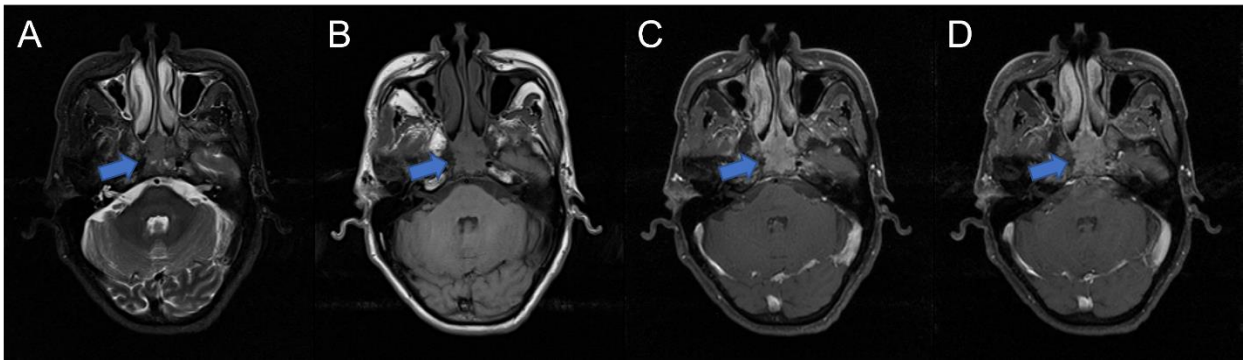

Figure 3. An example of VCE-MRI synthesis in a patient with head and neck cancer. A shows the T_2w MRI image. B shows the T_1w pre-contrast MRI image. C shows the real T_1w post-contrast MRI image. D shows the synthesized virtual T_1w post-contrast MRI image. The blue arrow shows the tumor position.

6 Conclusion

mpMRI techniques play an increasingly important role in RT, and there are exciting opportunities for novel research and development. To enable robust implementation, the study of mpMRI techniques should also endeavor to achieve standardization and quantification for efficient and effective treatment planning, delivery, and evaluation. Various novel MR techniques have shown promise in different RT applications and are worthy of further exploration.

7 Acknowledgement

This research was partly supported by a Research Scholar Grant from the American Cancer Society (RSG-15-137-01-CCE), research grants from the National Cancer Institute of the National Institutes of Health (R01 CA204189, R01 CA226899), General Research Fund from the University Grants Committee (GRF 15102118, GRF 15102219) and Health and Medical Research Fund from the Food and Health Bureau (HMRF 07183266), The Government of the Hong Kong Special Administrative Region. The content is solely the responsibility of the authors and does not necessarily represent the official views of the funding agents.

References

1. Torresin A, Brambilla MG, Monti AF, et al. Review of potential improvements using MRI in the radiotherapy workflow. *Z Med Phys.* 2015;25(3):210-220.
2. Gurney-Champion OJ, Mahmood F, van Schie M, et al. Quantitative imaging for radiotherapy purposes. *Radiother Oncol.* 2020;146:66-75.
3. Paganelli C, Whelan B, Peroni M, et al. MRI-guidance for motion management in external beam radiotherapy: current status and future challenges. *Physics in medicine and biology.* 2018;63(22):22tr03.
4. Leibfarth S, Winter RM, Lyng H, Zips D, Thorwarth D. Potentials and challenges of diffusion-weighted magnetic resonance imaging in radiotherapy. *Clin Transl Radiat Oncol.* 2018;13:29-37.
5. Winfield JM, Payne GS, Weller A, deSouza NM. DCE-MRI, DW-MRI, and MRS in Cancer: Challenges and Advantages of Implementing Qualitative and Quantitative Multi-parametric Imaging in the Clinic. *Top Magn Reson Imaging.* 2016;25(5):245-254.
6. Sanguineti G, Bertini L, Faiella A, et al. Response on DCE-MRI predicts outcome of salvage radiotherapy for local recurrence after radical prostatectomy. *Tumori.* 2021;107(1):55-63.
7. Ye C, Lin Q, Jin Z, Zheng C, Ma S. Predictive effect of DCE-MRI and DWI in brain metastases from NSCLC. *Open Med (Wars).* 2021;16(1):1265-1275.
8. Ma D, Gulani V, Seiberlich N, et al. Magnetic resonance fingerprinting. *Nature.* 2013;495(7440):187-192.
9. Korzdorfer G, Jiang Y, Speier P, et al. Magnetic resonance field fingerprinting. *Magn Reson Med.* 2019;81(4):2347-2359.
10. Heule R, Celicanin Z, Kozerke S, Bieri O. Simultaneous multislice triple-echo steady-state (SMS-TESS) T1 , T2 , PD, and off-resonance mapping in the human brain. *Magn Reson Med.* 2018;80(3):1088-1100.
11. Cheng CC, Preiswerk F, Hoge WS, Kuo TH, Madore B. Multipathway multi-echo (MPME) imaging: all main MR parameters mapped based on a single 3D scan. *Magn Reson Med.* 2019;81(3):1699-1713.
12. Benjamin P, Khan F, MacKinnon AD. The use of diffusion weighted imaging to evaluate pathology outside the brain parenchyma in neuroimaging studies. *Br J Radiol.* 2017;90(1072):20160821-20160821.
13. Partridge SC, Zhang Z, Newitt DC, et al. Diffusion-weighted MRI Findings Predict Pathologic Response in Neoadjuvant Treatment of Breast Cancer: The ACRIN 6698 Multicenter Trial. *Radiology.* 2018;289(3):618-627.
14. Kang SR, Kim HW, Kim HS. Evaluating the Relationship Between Dynamic Contrast-Enhanced MRI (DCE-MRI) Parameters and Pathological Characteristics in Breast Cancer. *Journal of magnetic resonance imaging : JMRI.* 2020;52(5):1360-1373.
15. Liu C, Sun R, Wang J, et al. Combination of DCE-MRI and DWI in Predicting the Treatment Effect of Concurrent Chemoradiotherapy in Esophageal Carcinoma. *Biomed Res Int.* 2020;2020:2576563-2576563.
16. Kinh Do R, Reyngold M, Paudyal R, et al. Diffusion-Weighted and Dynamic Contrast-Enhanced MRI Derived Imaging Metrics for Stereotactic Body Radiotherapy of Pancreatic Ductal Adenocarcinoma: Preliminary Findings. *Tomography (Ann Arbor, Mich).* 2020;6(2):261-271.

17. Lee JH, Yoo GS, Yoon YC, Park HC, Kim HS. Diffusion-weighted and dynamic contrast-enhanced magnetic resonance imaging after radiation therapy for bone metastases in patients with hepatocellular carcinoma. *Scientific Reports.* 2021;11(1):10459.
18. Feng Y, Liu H, Ding Y, et al. Combined dynamic DCE-MRI and diffusion-weighted imaging to evaluate the effect of neoadjuvant chemotherapy in cervical cancer. *Tumori.* 2020;106(2):155-164.
19. Reig B, Heacock L, Geras KJ, Moy L. Machine learning in breast MRI. *Journal of magnetic resonance imaging : JMRI.* 2020;52(4):998-1018.
20. Cuocolo R, Cipullo MB, Stanzione A, et al. Machine learning applications in prostate cancer magnetic resonance imaging. *Eur Radiol Exp.* 2019;3(1):35.
21. Angulakshmi M, Deepa M. A Review on Deep Learning Architecture and Methods for MRI Brain Tumour Segmentation. *Curr Med Imaging.* 2021;17(6):695-706.
22. Lundervold AS, Lundervold A. An overview of deep learning in medical imaging focusing on MRI. *Zeitschrift für Medizinische Physik.* 2019;29(2):102-127.
23. Chandra SS, Bran Lorenzana M, Liu X, Liu S, Bollmann S, Crozier S. Deep learning in magnetic resonance image reconstruction. *J Med Imaging Radiat Oncol.* 2021;65(5):564-577.
24. Winkel DJ, Heye TJ, Benz MR, et al. Compressed Sensing Radial Sampling MRI of Prostate Perfusion: Utility for Detection of Prostate Cancer. *Radiology.* 2019;290(3):702-708.
25. Hollingsworth KG. Reducing acquisition time in clinical MRI by data undersampling and compressed sensing reconstruction. *Physics in medicine and biology.* 2015;60(21):R297-322.
26. Montalt-Tordera J, Muthurangu V, Hauptmann A, Steeden JA. Machine learning in Magnetic Resonance Imaging: Image reconstruction. *Phys Med.* 2021;83:79-87.
27. Devic S. MRI simulation for radiotherapy treatment planning. *Med Phys.* 2012;39(11):6701-6711.
28. Liney GP, Moerland MA. Magnetic Resonance Imaging Acquisition Techniques for Radiotherapy Planning. *Seminars in Radiation Oncology.* 2014;24(3):160-168.
29. Witt JS, Rosenberg SA, Bassetti MF. MRI-guided adaptive radiotherapy for liver tumours: visualising the future. *The Lancet Oncology.* 2020;21(2):e74-e82.
30. Maziero D, Straza MW, Ford JC, et al. MR-Guided Radiotherapy for Brain and Spine Tumors. *Front Oncol.* 2021;11:626100.
31. Pollard JM, Wen Z, Sadagopan R, Wang J, Ibbott GS. The future of image-guided radiotherapy will be MR guided. *Br J Radiol.* 2017;90(1073):20160667.
32. Lachance C, McCormack S. CADTH Rapid Response Reports. In: *Magnetic Resonance Imaging Simulators for Simulation and Treatment for Patients Requiring Radiation Therapy: A Review of the Clinical Effectiveness, Cost-Effectiveness, and Guidelines.* Ottawa (ON): Canadian Agency for Drugs and Technologies in Health. 2019.
33. Glide-Hurst CK, Paulson ES, McGee K, et al. Task group 284 report: magnetic resonance imaging simulation in radiotherapy: considerations for clinical implementation, optimization, and quality assurance. *Med Phys.* 2021;48(7):e636-e670.
34. Jafar MM, Reeves J, Ruthven MA, et al. Assessment of a carbon fibre MRI flatbed insert for radiotherapy treatment planning. *Br J Radiol.* 2016;89(1062):20160108.

35. McGee KP, Stormont RS, Lindsay SA, et al. Characterization and evaluation of a flexible MRI receive coil array for radiation therapy MR treatment planning using highly decoupled RF circuits. *Physics in medicine and biology.* 2018;63(8):08nt02.
36. Sun J, Pichler P, Dowling J, et al. MR simulation for prostate radiation therapy: effect of coil mounting position on image quality. *Br J Radiol.* 2014;87(1042):20140325.
37. Hoogcarspel SJ, Zijlema SE, Tijssen RHN, et al. Characterization of the first RF coil dedicated to 1.5 T MR guided radiotherapy. *Physics in medicine and biology.* 2018;63(2):025014.
38. Chandarana H, Wang H, Tijssen RHN, Das IJ. Emerging role of MRI in radiation therapy. *Journal of magnetic resonance imaging : JMRI.* 2018;48(6):1468-1478.
39. Han X. MR-based synthetic CT generation using a deep convolutional neural network method. *Med Phys.* 2017;44(4):1408-1419.
40. Gupta D, Kim M, Vineberg KA, Balter JM. Generation of Synthetic CT Images From MRI for Treatment Planning and Patient Positioning Using a 3-Channel U-Net Trained on Sagittal Images. *Frontiers in Oncology.* 2019;9.
41. Hsu S-H, DuPre P, Peng Q, Tomé WA. A technique to generate synthetic CT from MRI for abdominal radiotherapy. *J Appl Clin Med Phys.* 2020;21(2):136-143.
42. Heerkens HD, Hall WA, Li XA, et al. Recommendations for MRI-based contouring of gross tumor volume and organs at risk for radiation therapy of pancreatic cancer. *Pract Radiat Oncol.* 2017;7(2):126-136.
43. Paulson ES, Erickson B, Schultz C, Allen Li X. Comprehensive MRI simulation methodology using a dedicated MRI scanner in radiation oncology for external beam radiation treatment planning. *Med Phys.* 2015;42(1):28-39.
44. Di Tucci AA, Matta G, Deplano S, et al. Myocardial iron overload assessment by T2* magnetic resonance imaging in adult transfusion dependent patients with acquired anemias. *Haematologica.* 2008;93(9):1385-1388.
45. Wu G, Xi G, Hua Y, Sagher O. T2* magnetic resonance imaging sequences reflect brain tissue iron deposition following intracerebral hemorrhage. *Transl Stroke Res.* 2010;1(1):31-34.
46. Cuenod CA, Balvay D. Perfusion and vascular permeability: Basic concepts and measurement in DCE-CT and DCE-MRI. *Diagnostic and Interventional Imaging.* 2013;94(12):1187-1204.
47. Gordon Y, Partovi S, Müller-Eschner M, et al. Dynamic contrast-enhanced magnetic resonance imaging: fundamentals and application to the evaluation of the peripheral perfusion. *Cardiovasc Diagn Ther.* 2014;4(2):147-164.
48. Xie Y, Zhao J, Zhang P. A multicompartment model for intratumor tissue-specific analysis of DCE-MRI using non-negative matrix factorization. *Med Phys.* 2021;48(5):2400-2411.
49. Zahra MA, Hollingsworth KG, Sala E, Lomas DJ, Tan LT. Dynamic contrast-enhanced MRI as a predictor of tumour response to radiotherapy. *The Lancet Oncology.* 2007;8(1):63-74.
50. Ota Y, Liao E, Kurokawa R, et al. Diffusion-weighted and dynamic contrast-enhanced MRI to assess radiation therapy response for head and neck paragangliomas. *Journal of neuroimaging : official journal of the American Society of Neuroimaging.* 2021;31(5):1035-1043.

51. Mui AWL, Lee AWM, Lee VHF, et al. Prognostic and therapeutic evaluation of nasopharyngeal carcinoma by dynamic contrast-enhanced (DCE), diffusion-weighted (DW) magnetic resonance imaging (MRI) and magnetic resonance spectroscopy (MRS). *Magnetic Resonance Imaging.* 2021;83:50-56.
52. Muto M, Frauenfelder G, Senese R, et al. Dynamic susceptibility contrast (DSC) perfusion MRI in differential diagnosis between radionecrosis and neoangiogenesis in cerebral metastases using rCBV, rCBF and K2. *La radiologia medica.* 2018;123(7):545-552.
53. Thomsen HS. Nephrogenic systemic fibrosis: A serious late adverse reaction to gadodiamide. *European radiology.* 2006;16(12):2619-2621.
54. Moser FG, Watterson CT, Weiss S, et al. High Signal Intensity in the Dentate Nucleus and Globus Pallidus on Unenhanced T1-Weighted MR Images: Comparison between Gadobutrol and Linear Gadolinium-Based Contrast Agents. *AJNR American journal of neuroradiology.* 2018;39(3):421-426.
55. Nguyen NC, Molnar TT, Cummin LG, Kanal E. Dentate Nucleus Signal Intensity Increases Following Repeated Gadobenate Dimeglumine Administrations: A Retrospective Analysis. *Radiology.* 2020;296(1):122-130.
56. Le Bihan D, Breton E. Imagerie de diffusion in vivo par résonance magnétique nucléaire. *Comptes rendus de l'Académie des sciences Série 2, Mécanique, Physique, Chimie, Sciences de l'univers, Sciences de la Terre.* 1985;301(15):1109-1112.
57. Merboldt K-D, Hanicke W, Frahm J. Self-diffusion NMR imaging using stimulated echoes. *Journal of Magnetic Resonance (1969).* 1985;64(3):479-486.
58. Tsien C, Cao Y, Chenevert T. Clinical applications for diffusion magnetic resonance imaging in radiotherapy. *Seminars in radiation oncology.* 2014;24(3):218-226.
59. Baliyan V, Das CJ, Sharma R, Gupta AK. Diffusion weighted imaging: Technique and applications. *World J Radiol.* 2016;8(9):785-798.
60. Taylor DG, Bushell MC. The spatial mapping of translational diffusion coefficients by the NMR imaging technique. *Physics in medicine and biology.* 1985;30(4):345-349.
61. Papaevangelou E, Almeida GS, Jamin Y, Robinson SP, deSouza NM. Diffusion-weighted MRI for imaging cell death after cytotoxic or apoptosis-inducing therapy. *Br J Cancer.* 2015;112(9):1471-1479.
62. Thoeny HC, Ross BD. Predicting and monitoring cancer treatment response with diffusion-weighted MRI. *Journal of magnetic resonance imaging : JMRI.* 2010;32(1):2-16.
63. Foltz WD, Wu A, Chung P, et al. Changes in apparent diffusion coefficient and T2 relaxation during radiotherapy for prostate cancer. *Journal of magnetic resonance imaging : JMRI.* 2013;37(4):909-916.
64. Harry VN, Semple SI, Gilbert FJ, Parkin DE. Diffusion-weighted magnetic resonance imaging in the early detection of response to chemoradiation in cervical cancer. *Gynecol Oncol.* 2008;111(2):213-220.
65. Rizzo S, Buscarino V, Origgi D, et al. Evaluation of diffusion-weighted imaging (DWI) and MR spectroscopy (MRS) as early response biomarkers in cervical cancer patients. *La radiologia medica.* 2016;121(11):838-846.
66. Harry VN, Semple SI, Gilbert FJ, Parkin DE. Diffusion-weighted magnetic resonance imaging in the early detection of response to chemoradiation in cervical cancer. *Gynecologic Oncology.* 2008;111(2):213-220.

67. liu L, Wu N, Ouyang H, Dai JR, Wang WH. Diffusion-weighted MRI in early assessment of tumour response to radiotherapy in high-risk prostate cancer. *Br J Radiol.* 2014;87(1043):20140359.
68. Overgaard J, Horsman MR. Modification of hypoxia-induced radioresistance in tumors by the use of oxygen and sensitizers. *Seminars in Radiation Oncology.* 1996;6(1):10-21.
69. Chapman JD, Engelhardt EL, Stobbe CC, Schneider RF, Hanks GE. Measuring hypoxia and predicting tumor radioresistance with nuclear medicine assays. *Radiotherapy and Oncology.* 1998;46(3):229-237.
70. Carlson DJ, Yenice KM, Orton CG. Tumor hypoxia is an important mechanism of radioresistance in hypofractionated radiotherapy and must be considered in the treatment planning process. *Med Phys.* 2011;38(12):6347-6350.
71. O'Connor JPB, Robinson SP, Waterton JC. Imaging tumour hypoxia with oxygen-enhanced MRI and BOLD MRI. *Br J Radiol.* 2019;92(1095):20180642-20180642.
72. White DA, Zhang Z, Li L, et al. Developing oxygen-enhanced magnetic resonance imaging as a prognostic biomarker of radiation response. *Cancer Letters.* 2016;380(1):69-77.
73. Zha W, Kruger SJ, Johnson KM, et al. Pulmonary ventilation imaging in asthma and cystic fibrosis using oxygen-enhanced 3D radial ultrashort echo time MRI. *Journal of Magnetic Resonance Imaging.* 2018;47(5):1287-1297.
74. *Quantitative Imaging Biomarkers Alliance Profiles. Available from: http://qibawiki.rsna.org/index.php/Profiles*.
75. Chenevert TL, Galbán CJ, Ivancevic MK, et al. Diffusion coefficient measurement using a temperature-controlled fluid for quality control in multicenter studies. *J Magn Reson Imaging.* 2011;34(4):983-987.
76. Russek SE, Boss M, Jackson EF, et al. Characterization of NIST/ISMRM MRI System Phantom. Paper presented at: ISMRM 20th Annual Meeting and Exhibition, 5-11 May, 2012, Melbourne, Australia.
77. Jiang Y, Ma D, Keenan KE, Stupic KF, Gulani V, Griswold MA. Repeatability of magnetic resonance fingerprinting T1 and T2 estimates assessed using the ISMRM/NIST MRI system phantom. *Magn Reson Med.* 2017;78(4):1452-1457.
78. Keenan KE, Boss M, Jackson EF, Kown S, Jennings D, Russek S. NIST/ISMRM MRI system phantom T1 measurements on multiple MRI systems. Paper presented at: 21st Annual Meeting of ISMRM, Salt Lake City, Utah, USA, 2013.
79. Kumar NM, Fritz B, Stern SE, Warntjes JBM, Lisa Chuah YM, Fritz J. Synthetic MRI of the Knee: Phantom Validation and Comparison with Conventional MRI. *Radiology.* 2018;289(2):465-477.
80. van Houdt PJ, Kallehauge JF, Tanderup K, et al. Phantom-based quality assurance for multicenter quantitative MRI in locally advanced cervical cancer. *Radiother Oncol.* 2020;153:114-121.
81. Nejad-Davarani SP, Zakariaei N, Chen Y, et al. Rapid multicontrast brain imaging on a 0.35T MR-linac. *Med Phys.* 2020;47(9):4064-4076.
82. Kooreman ES, van Houdt PJ, Nowee ME, et al. Feasibility and accuracy of quantitative imaging on a 1.5 T MR-linear accelerator. *Radiotherapy and Oncology.* 2019;133:156-162.
83. Gopalan K, Tamir JI, Arias AC, Lustig M. Quantitative anatomy mimicking slice phantoms. *Magn Reson Med.* 2021;86(2):1159-1166.

84. Chen J, Daniel BL, Pauly KB. Investigation of proton density for measuring tissue temperature. *J Magn Reson Imaging.* 2006;23(3):430-434.
85. Smith G, Carpenter J-P, Mohiaddin R, Pennell D, Firmin D. A phantom study of temperature-dependent MRI T2* measurement. *Journal of Cardiovascular Magnetic Resonance.* 2009;11.
86. Malyarenko D, Galbán CJ, Londy FJ, et al. Multi-system repeatability and reproducibility of apparent diffusion coefficient measurement using an ice-water phantom. *J Magn Reson Imaging.* 2013;37(5):1238-1246.
87. Belli G, Busoni S, Ciccarone A, et al. Quality assurance multicenter comparison of different MR scanners for quantitative diffusion-weighted imaging. *J Magn Reson Imaging.* 2016;43(1):213-219.
88. Bane O, Hectors SJ, Wagner M, et al. Accuracy, repeatability, and interplatform reproducibility of T(1) quantification methods used for DCE-MRI: Results from a multicenter phantom study. *Magn Reson Med.* 2018;79(5):2564-2575.
89. Shridhar Konar A, Qian E, Geethanath S, et al. Quantitative imaging metrics derived from magnetic resonance fingerprinting using ISMRM/NIST MRI system phantom: An international multicenter repeatability and reproducibility study. *Med Phys.* 2021;48(5):2438-2447.
90. Price RG, Knight RA, Hwang KP, Bayram E, Nejad-Davarani SP, Glide-Hurst CK. Optimization of a novel large field of view distortion phantom for MR-only treatment planning. *Journal of applied clinical medical physics.* 2017;18(4):51-61.
91. Wang D, Strugnell W, Cowin G, Doddrell DM, Slaughter R. Geometric distortion in clinical MRI systems Part I: evaluation using a 3D phantom. *Magnetic resonance imaging.* 2004;22(9):1211-1221.
92. Walker A, Liney G, Metcalfe P, Holloway L. MRI distortion: considerations for MRI based radiotherapy treatment planning. *Australasian physical & engineering sciences in medicine / supported by the Australasian College of Physical Scientists in Medicine and the Australasian Association of Physical Sciences in Medicine.* 2014;37(1):103-113.
93. Hasler SW, Bernchou U, Bertelsen A, et al. Tumor-site specific geometric distortions in high field integrated magnetic resonance linear accelerator radiotherapy. *Physics and Imaging in Radiation Oncology.* 2020;15:100-104.
94. Jamtheim Gustafsson C. *MRI-Only Radiotherapy of Prostate Cancer: Development and Evaluation of Methods to Assess Fiducial Marker Detection, Geometric Accuracy and Dosimetric Integrity* 2019.
95. Putz F, Mengling V, Perrin R, et al. Magnetic resonance imaging for brain stereotactic radiotherapy: A review of requirements and pitfalls. *Strahlentherapie und Onkologie.* 2020;196(5):444-456.
96. Ellingson BM, Bendszus M, Boxerman J, et al. Consensus recommendations for a standardized Brain Tumor Imaging Protocol in clinical trials. *Neuro-Oncology.* 2015;17(9):1188-1198.
97. Danieli L, Riccitelli GC, Distefano D, et al. Brain Tumor-enhancement visualization and morphometric assessment: A comparison of MPRAGE, SPACE, and VIBE MRI techniques. *American Journal of Neuroradiology.* 2019;40(7):1140-1148.
98. Chappell PM, Pelc NJ, Foo TKF, Glover GH, Haros SP, Enzmann DR. Comparison of lesion enhancement on spin-echo and gradient-echo images. *American Journal of Neuroradiology.* 1994;15(1):37-44.

99. Reichert M, Morelli JN, Runge VM, et al. Contrast-enhanced 3-dimensional SPACE versus MP-RAGE for the detection of brain metastases: Considerations with a 32-channel head coil. *Investigative Radiology.* 2013;48(1):55-60.
100. Komada T, Naganawa S, Ogawa H, et al. Contrast-enhanced MR imaging of metastatic brain tumor at 3 Tesla: Utility of T1-weighted SPACE compared with 2D spin echo and 3D gradient echo sequence. *Magnetic Resonance in Medical Sciences.* 2008;7(1):13-21.
101. Yuh WTC, Tali ET, Nguyen HD, Simonson TM, Mayr NA, Fisher DJ. The effect of contrast dose, imaging time, and lesion size in the MR detection of intracerebral metastasis. *American Journal of Neuroradiology.* 1995;16(2):373-380.
102. Kushnirsky M, Nguyen V, Katz JS, et al. Time-delayed contrast-enhanced MRI improves detection of brain metastases and apparent treatment volumes. *Journal of Neurosurgery.* 2016;124(2):489-495.
103. Anzalone N, Essig M, Lee SK, et al. Optimizing contrast-enhanced magnetic resonance imaging characterization of brain metastases: Relevance to stereotactic radiosurgery. *Neurosurgery.* 2013;72(5):691-701.
104. Wong KH, Panek R, Bhide SA, Nutting CM, Harrington KJ, Newbold KL. The emerging potential of magnetic resonance imaging in personalizing radiotherapy for head and neck cancer: An oncologist's perspective. *British Journal of Radiology.* 2017;90(1071).
105. Chawla S, Kim S, Wang S, Poptani H. Diffusion-weighted imaging in head and neck cancers. *Future Oncology.* 2009;5(7):959-975.
106. Schakel T, Hoogduin JM, Terhaard CHJ, Philippens MEP. Diffusion weighted MRI in head-and-neck cancer: Geometrical accuracy. *Radiotherapy and Oncology.* 2013;109(3):394-397.
107. Yu JY, Zhang D, Huang XL, et al. Quantitative Analysis of DCE-MRI and RESOLVE-DWI for Differentiating Nasopharyngeal Carcinoma from Nasopharyngeal Lymphoid Hyperplasia. *J Med Syst.* 2020;44(4):75.
108. Cardoso M, Min M, Jameson M, et al. Evaluating diffusion-weighted magnetic resonance imaging for target volume delineation in head and neck radiotherapy. *J Med Imaging Radiat Oncol.* 2019;63(3):399-407.
109. Stieb S, Elgohari B, Fuller CD. Repetitive MRI of organs at risk in head and neck cancer patients undergoing radiotherapy. *Clin Transl Radiat Oncol.* 2019;18:131-139.
110. Biederer J, Beer M, Hirsch W, et al. MRI of the lung (2/3). Why … when … how? *Insights Imaging.* 2012;3(4):355-371.
111. Menten MJ, Wetscherek A, Fast MF. MRI-guided lung SBRT: Present and future developments. *Physica Medica.* 2017;44:139-149.
112. Puderbach M, Hintze C, Ley S, Eichinger M, Kauczor HU, Biederer J. MR imaging of the chest: A practical approach at 1.5 T. *European Journal of Radiology.* 2007;64(3):345-355.
113. Zou Y, Zhang M, Wang Q, Shang D, Wang L, Yu G. Quantitative investigation of solitary pulmonary nodules: Dynamic contrast-enhanced MRI and histopathologic analysis. *American Journal of Roentgenology.* 2008;191(1):252-259.
114. Chen L, Zhang J, Bao J, et al. Meta-analysis of diffusion-weighted MRI in the differential diagnosis of lung lesions. *Journal of Magnetic Resonance Imaging.* 2013;37(6):1351-1358.

115. Kumar S, Rai R, Stemmer A, et al. Feasibility of free breathing Lung MRI for Radiotherapy using non-Cartesian k-space acquisition schemes. *Br J Radiol.* 2017;90(1080):20170037-20170037.
116. Ahn KH, Hargreaves BA, Alley MT, et al. MRI guidance for accelerated partial breast irradiation in prone position: imaging protocol design and evaluation. *Int J Radiat Oncol Biol Phys.* 2009;75(1):285-293.
117. Pogson EM, Delaney GP, Ahern V, et al. Comparison of Magnetic Resonance Imaging and Computed Tomography for Breast Target Volume Delineation in Prone and Supine Positions. *Int J Radiat Oncol Biol Phys.* 2016;96(4):905-912.
118. Groot Koerkamp ML, Vasmel JE, Russell NS, et al. Optimizing MR-Guided Radiotherapy for Breast Cancer Patients. *Front Oncol.* 2020;10:1107.
119. Tanaka O, Yagi N, Tawada M, et al. Hemostatic Radiotherapy for Gastric Cancer: MRI as an Alternative to Endoscopy for Post-Treatment Evaluation. *J Gastrointest Cancer.* 2022. doi: 10.1007/s12029-022-00837-9.
120. Zhang Y, Yu J. The role of MRI in the diagnosis and treatment of gastric cancer. *Diagnostic and interventional radiology (Ankara, Turkey).* 2020;26(3):176-182.
121. Ghai S, Haider MA. Multiparametric-MRI in diagnosis of prostate cancer. *Indian J Urol.* 2015;31(3):194-201.
122. Salembier C, Villeirs G, De Bari B, et al. ESTRO ACROP consensus guideline on CT- and MRI-based target volume delineation for primary radiation therapy of localized prostate cancer. *Radiotherapy and Oncology.* 2018;127(1):49-61.
123. Chen HH, Lin PT, Kuo LT, Lin KS, Fang CC, Chi CC. Bladder volume reproducibility after water consumption in patients with prostate cancer undergoing radiotherapy: A systematic review and meta-analysis. *Biomed J.* 2021;44(6 Suppl 2):S226-s234.
124. O'Doherty UM, McNair HA, Norman AR, et al. Variability of bladder filling in patients receiving radical radiotherapy to the prostate. *Radiother Oncol.* 2006;79(3):335-340.
125. Fujioka C, Ishii K, Yamanaga T, et al. Optimal bladder volume at treatment planning for prostate cancer patients receiving volumetric modulated arc therapy. *Pract Radiat Oncol.* 2016;6(6):395-401.
126. Jadon R, Pembroke CA, Hanna CL, et al. A Systematic Review of Organ Motion and Image-guided Strategies in External Beam Radiotherapy for Cervical Cancer. *Clinical Oncology.* 2014;26(4):185-196.
127. Ma S, Zhang T, Jiang L, et al. Impact of bladder volume on treatment planning and clinical outcomes of radiotherapy for patients with cervical cancer. *Cancer Manag Res.* 2019;11:7171-7181.
128. Keall PJM, Gig S. Balter, James M. Emery, Richard S. Forster, Kenneth M. Jiang, Steve B. Kapatoes, Jeffrey M. Low, Daniel A. Murphy, Martin J. Murray, Brad R. Ramsey, Chester R. Van Herk, Marcel B. Vedam, S. Sastry Wong, John W. Yorke, Ellen The management of respiratory motion in radiation oncology report of AAPM Task Group 76. *Med Phys.* 2006;33:27.
129. Stevens CW, Munden RF, Forster KM, et al. Respiratory-driven lung tumor motion is independent of tumor size, tumor location, and pulmonary function. *International Journal of Radiation Oncology Biology Physics.* 2001;51(1):62-68.
130. Brandner ED, Chetty IJ, Giaddui TG, Xiao Y, Huq MS. Motion management strategies and technical issues associated with stereotactic body radiotherapy of thoracic and upper abdominal tumors: A review from NRG oncology. *Med Phys.* 2017;44(6):2595-2612.

131. Case RB, Moseley DJ, Sonke JJ, et al. Interfraction and intrafraction changes in amplitude of breathing motion in stereotactic liver radiotherapy. *Int J Radiat Oncol Biol Phys.* 2010;77(3):918-925.
132. Yang J, Cai J, Wang H, et al. Is diaphragm motion a good surrogate for liver tumor motion? *Int J Radiat Oncol Biol Phys.* 2014;90(4):952-958.
133. Park JC, Park SH, Kim JH, et al. Liver motion during cone beam computed tomography guided stereotactic body radiation therapy. *Med Phys.* 2012;39(10):6431-6442.
134. Shirato H, Shimizu S, Kunieda T, et al. Physical aspects of a real-time tumor-tracking system for gated radiotherapy. *International Journal of Radiation Oncology Biology Physics.* 2000;48(4):1187-1195.
135. Minohara S, Kanai T, Endo M, Noda K, Kanazawa M. Respiratory gated irradiation system for heavy-ion radiotherapy. *International Journal of Radiation Oncology Biology Physics.* 2000;47(4):1097-1103.
136. Murphy MJ, Adler JR, Jr., Bodduluri M, et al. Image-guided radiosurgery for the spine and pancreas. *Computer Aided Surgery.* 2000;5(4):278-288.
137. Cai J, Read PW, Larner JM, Jones DR, Benedict SH, Sheng K. Reproducibility of Interfraction Lung Motion Probability Distribution Function Using Dynamic Mri: Statistical Analysis. *Int J Radiat Oncol.* 2008;72(4):1228-1235.
138. Barnes EA, Murray BR, Robinson DM, Underwood LJ, Hanson J, Roa WHY. Dosimetric evaluation of lung tumor immobilization using breath hold at deep inspiration. *International Journal of Radiation Oncology Biology Physics.* 2001;50(4):1091-1098.
139. Chen QS, Weinhous MS, Deibel FC, Ciezki JP, Macklis RM. Fluoroscopic study of tumor motion due to breathing: Facilitating precise radiation therapy for lung cancer patients. *Medical Physics.* 2001;28(9):1850-1856.
140. Grills IS, Yan D, Martinez AA, Vicini FA, Wong JW, Kestin LL. Potential for reduced toxicity and dose escalation in the treatment of inoperable non-small-cell lung cancer: A comparison of intensity-modulated radiation therapy (IMRT), 3D conformal radiation, and elective nodal irradiation. *International Journal of Radiation Oncology Biology Physics.* 2003;57(3):875-890.
141. Dinkel J, Hintze C, Tetzlaff R, et al. 4D-MRI analysis of lung tumor motion in patients with hemidiaphragmatic paralysis. *Radiother Oncol.* 2009;91(3):449-454.
142. Thomas DH, Santhanam A, Kishan AU, et al. Initial clinical observations of intra- and interfractional motion variation in MR-guided lung SBRT. *Br J Radiol.* 2018;91(1083):20170522.
143. Yang W, Fan Z, Deng Z, et al. Novel 4D-MRI of tumor infiltrating vasculature: characterizing tumor and vessel volume motion for selective boost volume definition in pancreatic radiotherapy. *Radiation oncology (London, England).* 2018;13(1):191.
144. Akino Y, Oh RJ, Masai N, Shiomi H, Inoue T. Evaluation of potential internal target volume of liver tumors using cine-MRI. *Med Phys.* 2014;41(11):111704.
145. Nonaka H, Onishi H, Watanabe M, Nam VH. Assessment of abdominal organ motion using cine magnetic resonance imaging in different gastric motilities: a comparison between fasting and postprandial states. *Journal of radiation research.* 2019;60(6):837-843.
146. Zhou Y, Yuan J, Wong OL, et al. Assessment of positional reproducibility in the head and neck on a 1.5-T MR simulator for an offline MR-guided radiotherapy solution. *Quantitative imaging in medicine and surgery.* 2018;8(9):925-935.

147. Glockner JF, Hu HH, Stanley DW, Angelos L, King K. Parallel MR imaging: A user's guide. *Radiographics.* 2005;25(5):1279-1297.
148. Deshmane A, Gulani V, Griswold MA, Seiberlich N. Parallel MR imaging. *Journal of Magnetic Resonance Imaging.* 2012;36(1):55-72.
149. Winkler SA, Corea J, Lechêne B, et al. Evaluation of a flexible 12-channel screenprinted pediatric MRI coil. *Radiology.* 2019;291(1):180-185.
150. Feng L, Benkert T, Block KT, Sodickson DK, Otazo R, Chandarana H. Compressed sensing for body MRI. *Journal of Magnetic Resonance Imaging.* 2017;45(4):966-987.
151. Otazo R, Kim D, Axel L, Sodickson DK. Combination of compressed sensing and parallel imaging for highly accelerated first-pass cardiac perfusion MRI. *Magnetic Resonance in Medicine.* 2010;64(3):767-776.
152. Chandarana H, Block TK, Rosenkrantz AB, et al. Free-breathing radial 3D fat-suppressed T1-weighted gradient echo sequence: A viable alternative for contrast-enhanced liver imaging in patients unable to suspend respiration. *Investigative Radiology.* 2011;46(10):648-653.
153. Barth M, Breuer F, Koopmans PJ, Norris DG, Poser BA. Simultaneous multislice (SMS) imaging techniques. *Magnetic Resonance in Medicine.* 2016;75(1):63-81.
154. Bilgic B, Setsompop K, Cohen-Adad J, Yendiki A, Wald LL, Adalsteinsson E. Accelerated diffusion spectrum imaging with compressed sensing using adaptive dictionaries. *Magnetic Resonance in Medicine.* 2012;68(6):1747-1754.
155. Serai SD, Hu HH, Ahmad R, et al. Newly Developed Methods for Reducing Motion Artifacts in Pediatric Abdominal MRI: Tips and Pearls. *AJR American journal of roentgenology.* 2020;214(5):1042-1053.
156. Serai SD, Rigsby CK, Kan HJ, Panigrahy A, Hernanz-Schulman M, Anupindi SA. Inclusion of Pediatric-Specific Indications and Procedures in the New ACR MRI Accreditation Program. *Journal of the American College of Radiology.* 2018;15(7):1022-1026.
157. Serai SD, Jones BV, Podberesky DJ, Coley B. Is it time for a dedicated pediatric MRI ACR accreditation program? *Journal of the American College of Radiology.* 2013;10(4):274-278.
158. Barrera CA, Otero HJ, Hartung HD, Biko DM, Serai SD. Protocol optimization for cardiac and liver iron content assessment using MRI: What sequence should I use? *Clinical Imaging.* 2019;56:52-57.
159. Tang Y, Yamashita Y, Namimoto T, Abe Y, Takahashi M. Liver T2-weighted MR imaging: Comparison of fast and conventional half- Fourier single-shot turbo spin-echo, breath-hold turbo spin-echo, and respiratory-triggered turbo spin-echo sequences. *Radiology.* 1997;203(3):766-772.
160. Yu JS, Kim KW, Kim YH, Jeong EK, Chien D. Comparison of multishot turbo spin echo and HASTE sequences for T2- weighted MRI of liver lesions. *Journal of Magnetic Resonance Imaging.* 1998;8(5):1079-1084.
161. Feng L, Axel L, Chandarana H, Block KT, Sodickson DK, Otazo R. XD-GRASP: Golden-angle radial MRI with reconstruction of extra motion-state dimensions using compressed sensing. *Magnetic Resonance in Medicine.* 2016;75(2):775-788.
162. Ippoliti M, Lukas M, Brenner W, Schaeffter T, Makowski MR, Kolbitsch C. 3D nonrigid motion correction for quantitative assessment of hepatic lesions in DCE-MRI. *Magn Reson Med.* 2019;82(5):1753-1766.

163. Zhang T, Cheng JY, Potnick AG, et al. Fast pediatric 3D free-breathing abdominal dynamic contrast enhanced MRI with high spatiotemporal resolution. *Journal of Magnetic Resonance Imaging.* 2015;41(2):460-473.
164. Chandarana H, Feng L, Ream J, et al. Respiratory motion-resolved compressed sensing reconstruction of free-breathing radial acquisition for dynamic liver magnetic resonance imaging. *Investigative Radiology.* 2015;50(11):749-756.
165. Li Z, Hu HH, Miller JH, et al. A Spiral Spin-Echo MR Imaging Technique for Improved Flow Artifact Suppression in T1-Weighted Postcontrast Brain Imaging: A Comparison with Cartesian Turbo Spin-Echo. *American Journal of Neuroradiology.* 2016;37(4):642.
166. Zaitsev M, Maclaren J, Herbst M. Motion artifacts in MRI: A complex problem with many partial solutions. *Journal of Magnetic Resonance Imaging.* 2015;42(4):887-901.
167. Pipe JG. Motion correction with PROPELLER MRI: Application to head motion and free-breathing cardiac imaging. *Magnetic Resonance in Medicine.* 1999;42(5):963-969.
168. Delattre BMA, Heidemann RM, Crowe LA, Vallée JP, Hyacinthe JN. Spiral demystified. *Magnetic Resonance Imaging.* 2010;28(6):862-881.
169. Wielpütz M, Kauczor HU. MRI of the lung: state of the art. *Diagnostic and interventional radiology (Ankara, Turkey).* 2012;18(4):344-353.
170. Low RN, Gurney J. Diffusion-weighted MRI (DWI) in the oncology patient: Value of breathhold DWI compared to unenhanced and gadolinium-enhanced MRI. *Journal of Magnetic Resonance Imaging.* 2007;25(4):848-858.
171. Tamada D, Kromrey ML, Ichikawa S, Onishi H, Motosugi U. Motion Artifact Reduction Using a Convolutional Neural Network for Dynamic Contrast Enhanced MR Imaging of the Liver. *Magnetic resonance in medical sciences : MRMS : an official journal of Japan Society of Magnetic Resonance in Medicine.* 2020;19(1):64-76.
172. Higaki T, Nakamura Y, Tatsugami F, Nakaura T, Awai K. Improvement of image quality at CT and MRI using deep learning. *Japanese Journal of Radiology.* 2019;37(1):73-80.
173. Lin DJ, Johnson PM, Knoll F, Lui YW. Artificial Intelligence for MR Image Reconstruction: An Overview for Clinicians. *Journal of Magnetic Resonance Imaging.* 2020. doi: 10.1002/jmri.27078.
174. Han Y, Yoo J, Kim HH, Shin HJ, Sung K, Ye JC. Deep learning with domain adaptation for accelerated projection-reconstruction MR. *Magnetic Resonance in Medicine.* 2018;80(3):1189-1205.
175. Oksuz I, Ruijsink B, Puyol-Antón E, et al. Automatic CNN-based detection of cardiac MR motion artefacts using k-space data augmentation and curriculum learning. *Medical Image Analysis.* 2019;55:136-147.
176. Haskell MW, Cauley SF, Bilgic B, et al. Network Accelerated Motion Estimation and Reduction (NAMER): Convolutional neural network guided retrospective motion correction using a separable motion model. *Magnetic Resonance in Medicine.* 2019;82(4):1452-1461.
177. Stemkens B, Paulson ES, Tijssen RHN. Nuts and bolts of 4D-MRI for radiotherapy. *Physics in medicine and biology.* 2018;63(21):21tr01.
178. van de Lindt TN, Nowee ME, Janssen T, et al. Technical feasibility and clinical evaluation of 4D-MRI guided liver SBRT on the MR-linac. *Radiother Oncol.* 2022;167:285-291.

179. van de Lindt TN, Fast MF, van den Wollenberg W, et al. Validation of a 4D-MRI guided liver stereotactic body radiation therapy strategy for implementation on the MR-linac. *Physics in medicine and biology.* 2021;66(10).
180. Yuan J, Wong OL, Zhou Y, Chueng KY, Yu SK. A fast volumetric 4D-MRI with sub-second frame rate for abdominal motion monitoring and characterization in MRI-guided radiotherapy. *Quant Imaging Med Surg.* 2019;9(7):1303-1314.
181. Du D, Caruthers SD, Glide-Hurst C, et al. High-quality T2-weighted 4-dimensional magnetic resonance imaging for radiation therapy applications. *International Journal of Radiation Oncology Biology Physics.* 2015;92(2):430-437.
182. Rohlfing T, Maurer CR, Jr., O'Dell WG, Zhong J. Modeling liver motion and deformation during the respiratory cycle using intensity-based nonrigid registration of gated MR images. *Med Phys.* 2004;31(3):427-432.
183. Hu Y, Caruthers SD, Low DA, Parikh PJ, Mutic S. Respiratory amplitude guided 4-dimensional magnetic resonance imaging. *Int J Radiat Oncol Biol Phys.* 2013;86(1):198-204.
184. Xiao H, Ni R, Zhi S, et al. A dual-supervised deformation estimation model (DDEM) for constructing ultra-quality 4D-MRI based on a commercial low-quality 4D-MRI for liver cancer radiation therapy. *Med Phys.* 2022;49(5):3159-3170.
185. Glide-Hurst CK, Kim JP, To D, et al. Four dimensional magnetic resonance imaging optimization and implementation for magnetic resonance imaging simulation. *Pract Radiat Oncol.* 2015;5(6):433-442.
186. Li G, Wei J, Olek D, et al. Direct Comparison of Respiration-Correlated Four-Dimensional Magnetic Resonance Imaging Reconstructed Using Concurrent Internal Navigator and External Bellows. *Int J Radiat Oncol Biol Phys.* 2017;97(3):596-605.
187. Feng L. 4D Golden-Angle Radial MRI at Subsecond Temporal Resolution. *NMR Biomed.* 2022. doi: 10.1002/nbm.4844:e4844.
188. Liu YL, Yin FF, Chen NK, Chu ML, Cai J. Four dimensional magnetic resonance imaging with retrospective k-space reordering: A feasibility study. *Med Phys.* 2015;42(2):534-541.
189. Yang J, Cai J, Wang HJ, et al. Four-Dimensional Magnetic Resonance Imaging Using Axial Body Area as Respiratory Surrogate: Initial Patient Results. *Int J Radiat Oncol.* 2014;88(4):907-912.
190. Cai J, Chang Z, Wang Z, Paul Segars W, Yin FF. Four-dimensional magnetic resonance imaging (4D-MRI) using image-based respiratory surrogate: a feasibility study. *Med Phys.* 2011;38(12):6384-6394.
191. Liu Y, Yin FF, Czito BG, Bashir MR, Cai J. T2-weighted four dimensional magnetic resonance imaging with result-driven phase sorting. *Medical Physics.* 2015;42(8).
192. Buerger C, Clough RE, King AP, Schaeffter T, Prieto C. Nonrigid motion modeling of the liver from 3-D undersampled self-gated golden-radial phase encoded MRI. *IEEE Transactions on Medical Imaging.* 2012;31(3):805-815.
193. Zhang L, Yin FF, Li T, et al. Multi-contrast four-dimensional magnetic resonance imaging (MC-4D-MRI): Development and initial evaluation in liver tumor patients. *Med Phys.* 2021;48(12):7984-7997.
194. Breuer K, Meyer CB, Breuer FA, et al. Stable and efficient retrospective 4D-MRI using non-uniformly distributed quasi-random numbers. *Physics in medicine and biology.* 2018;63(7):075002.

195. Keijnemans K, Borman PTS, Uijtewaal P, Woodhead PL, Raaymakers BW, Fast MF. A hybrid 2D/4D-MRI methodology using simultaneous multislice imaging for radiotherapy guidance. *Med Phys.* 2022;49(9):6068-6081.
196. Keijnemans K, Borman PTS, van Lier A, Verhoeff JJC, Raaymakers BW, Fast MF. Simultaneous multi-slice accelerated 4D-MRI for radiotherapy guidance. *Physics in medicine and biology.* 2021;66(9).
197. Hancu I, Lee SK, Hulsey K, et al. Distortion correction in diffusion-weighted imaging of the breast: Performance assessment of prospective, retrospective, and combined (prospective + retrospective) approaches. *Magn Reson Med.* 2017;78(1):247-253.
198. Porter DA, Heidemann RM. High resolution diffusion-weighted imaging using readout-segmented echo-planar imaging, parallel imaging and a two-dimensional navigator-based reacquisition. *Magn Reson Med.* 2009;62(2):468-475.
199. Katahira K, Takahara T, Kwee TC, et al. Ultra-high-b-value diffusion-weighted MR imaging for the detection of prostate cancer: evaluation in 201 cases with histopathological correlation. *Eur Radiol.* 2011;21(1):188-196.
200. Kang Y, Choi SH, Kim YJ, et al. Gliomas: Histogram analysis of apparent diffusion coefficient maps with standard- or high-b-value diffusion-weighted MR imaging--correlation with tumor grade. *Radiology.* 2011;261(3):882-890.
201. Hauser T, Essig M, Jensen A, et al. Characterization and therapy monitoring of head and neck carcinomas using diffusion-imaging-based intravoxel incoherent motion parameters-preliminary results. *Neuroradiology.* 2013;55(5):527-536.
202. Jensen JH, Helpern JA, Ramani A, Lu H, Kaczynski K. Diffusional kurtosis imaging: the quantification of non-gaussian water diffusion by means of magnetic resonance imaging. *Magn Reson Med.* 2005;53(6):1432-1440.
203. Rata M, Collins DJ, Darcy J, et al. Assessment of repeatability and treatment response in early phase clinical trials using DCE-MRI: comparison of parametric analysis using MR- and CT-derived arterial input functions. *Eur Radiol.* 2016;26(7):1991-1998.
204. Tofts PS, Berkowitz B, Schnall MD. Quantitative analysis of dynamic Gd-DTPA enhancement in breast tumors using a permeability model. *Magnetic resonance in medicine : official journal of the Society of Magnetic Resonance in Medicine / Society of Magnetic Resonance in Medicine.* 1995;33(4):564-568.
205. Johnson TN, Rostami-Hodjegan A. Resurgence in the use of physiologically based pharmacokinetic models in pediatric clinical pharmacology: parallel shift in incorporating the knowledge of biological elements and increased applicability to drug development and clinical practice. *Paediatric anaesthesia.* 2011;21(3):291-301.
206. Tofts PS. Modeling tracer kinetics in dynamic Gd-DTPA MR imaging. *Journal of magnetic resonance imaging : JMRI.* 1997;7(1):91-101.
207. Brix G, Kiessling F, Lucht R, et al. Microcirculation and microvasculature in breast tumors: pharmacokinetic analysis of dynamic MR image series. *Magnetic resonance in medicine : official journal of the Society of Magnetic Resonance in Medicine / Society of Magnetic Resonance in Medicine.* 2004;52(2):420-429.
208. Bagher-Ebadian H, Jain R, Nejad-Davarani SP, et al. Model selection for DCE-T1 studies in glioblastoma. *Magnetic resonance in medicine : official journal of the Society of Magnetic Resonance in Medicine / Society of Magnetic Resonance in Medicine.* 2012;68(1):241-251.

209. Ewing JR, Bagher-Ebadian H. Model selection in measures of vascular parameters using dynamic contrast-enhanced MRI: experimental and clinical applications. *NMR in biomedicine.* 2013;26(8):1028-1041.
210. Barth BK, De Visschere PJL, Cornelius A, et al. Detection of Clinically Significant Prostate Cancer: Short Dual-Pulse Sequence versus Standard Multiparametric MR Imaging-A Multireader Study. *Radiology.* 2017;284(3):725-736.
211. Zeng J, Cheng Q, Zhang D, Fan M, Shi C, Luo L. Diagnostic Ability of Dynamic Contrast-Enhanced Magnetic Resonance Imaging for Prostate Cancer and Clinically Significant Prostate Cancer in Equivocal Lesions: A Systematic Review and Meta-Analysis. *Frontiers in Oncology.* 2021;11.
212. Lee J, Carver E, Feldman A, Pantelic MV, Elshaikh M, Wen N. Volumetric and Voxel-Wise Analysis of Dominant Intraprostatic Lesions on Multiparametric MRI. *Front Oncol.* 2019;9:616.
213. Wu J, Li B, Sun X, et al. Heterogeneous Enhancement Patterns of Tumor-adjacent Parenchyma at MR Imaging Are Associated with Dysregulated Signaling Pathways and Poor Survival in Breast Cancer. *Radiology.* 2017;285(2):401-413.
214. Gevaert O, Mitchell LA, Achrol AS, et al. Glioblastoma Multiforme: Exploratory Radiogenomic Analysis by Using Quantitative Image Features. *Radiology.* 2015;276(1):313.
215. Fehr D, Veeraraghavan H, Wibmer A, et al. Automatic classification of prostate cancer Gleason scores from multiparametric magnetic resonance images. *Proc Natl Acad Sci U S A.* 2015;112(46):E6265-6273.
216. Panda A, Mehta BB, Coppo S, et al. Magnetic Resonance Fingerprinting-An Overview. *Curr Opin Biomed Eng.* 2017;3:56-66.
217. Doneva M, Bornert P, Eggers H, Stehning C, Senegas J, Mertins A. Compressed sensing reconstruction for magnetic resonance parameter mapping. *Magn Reson Med.* 2010;64(4):1114-1120.
218. Liao C, Bilgic B, Manhard MK, et al. 3D MR fingerprinting with accelerated stack-of-spirals and hybrid sliding-window and GRAPPA reconstruction. *Neuroimage.* 2017;162:13-22.
219. Ma D, Jiang Y, Chen Y, et al. Fast 3D magnetic resonance fingerprinting for a whole-brain coverage. *Magn Reson Med.* 2018;79(4):2190-2197.
220. Su P, Mao D, Liu P, et al. Multiparametric estimation of brain hemodynamics with MR fingerprinting ASL. *Magn Reson Med.* 2017;78(5):1812-1823.
221. Buonincontri G, Sawiak SJ. MR fingerprinting with simultaneous B1 estimation. *Magn Reson Med.* 2016;76(4):1127-1135.
222. Cloos MA, Knoll F, Zhao T, et al. Multiparametric imaging with heterogeneous radiofrequency fields. *Nat Commun.* 2016;7:12445.
223. Christen T, Pannetier NA, Ni WW, et al. MR vascular fingerprinting: A new approach to compute cerebral blood volume, mean vessel radius, and oxygenation maps in the human brain. *Neuroimage.* 2014;89:262-270.
224. Lemasson B, Pannetier N, Coquery N, et al. MR Vascular Fingerprinting in Stroke and Brain Tumors Models. *Sci Rep.* 2016;6:37071.
225. Pouliot P, Gagnon L, Lam T, et al. Magnetic resonance fingerprinting based on realistic vasculature in mice. *Neuroimage.* 2017;149:436-445.

226. Rieger B, Zimmer F, Zapp J, Weingartner S, Schad LR. Magnetic resonance fingerprinting using echo-planar imaging: Joint quantification of T1 and T2 * relaxation times. *Magn Reson Med.* 2017;78(5):1724-1733.
227. Buonincontri G, Biagi L, Retico A, et al. Multi-site repeatability and reproducibility of MR fingerprinting of the healthy brain at 1.5 and 3.0T. *Neuroimage.* 2019;195:362-372.
228. Buonincontri G, Kurzawski JW, Kaggie JD, et al. Three dimensional MRF obtains highly repeatable and reproducible multi-parametric estimations in the healthy human brain at 1.5T and 3T. *Neuroimage.* 2021;226:117573.
229. O'Connor JP, Aboagye EO, Adams JE, et al. Imaging biomarker roadmap for cancer studies. *Nat Rev Clin Oncol.* 2017;14(3):169-186.
230. Ma D, Pierre EY, Jiang Y, et al. Music-based magnetic resonance fingerprinting to improve patient comfort during MRI examinations. *Magn Reson Med.* 2016;75(6):2303-2314.
231. Wang CY, Liu Y, Huang S, Griswold MA, Seiberlich N, Yu X. (31) P magnetic resonance fingerprinting for rapid quantification of creatine kinase reaction rate in vivo. *NMR Biomed.* 2017;30(12).
232. Dastmalchian S, Kilinc O, Onyewadume L, et al. Radiomic analysis of magnetic resonance fingerprinting in adult brain tumors. *Eur J Nucl Med Mol Imaging.* 2021;48(3):683-693.
233. Bai Y, Shen Y, Chen R, et al. Magnetic resonance fingerprinting for preoperative differentiation between gonadotroph and non-gonadotroph pituitary macroadenomas. *Eur Radiol.* 2021. doi: 10.1007/s00330-021-07950-6.
234. Chen Y, Chen MH, Baluyot KR, et al. MR fingerprinting enables quantitative measures of brain tissue relaxation times and myelin water fraction in the first five years of life. *Neuroimage.* 2019;186:782-793.
235. Badve C, Yu A, Rogers M. Simultaneous T1 and T2 brain relaxometry in asymptomatic volunteers using magnetic resonance fingerprinting. *Tomography.* 2015;1(2):136-144.
236. Ma D, Jones SE, Deshmane A, et al. Development of high-resolution 3D MR fingerprinting for detection and characterization of epileptic lesions. *J Magn Reson Imaging.* 2019;49(5):1333-1346.
237. Liao C, Wang K, Cao X, et al. Detection of Lesions in Mesial Temporal Lobe Epilepsy by Using MR Fingerprinting. *Radiology.* 2018;288(3):804-812.
238. Lu L, Chen Y, Shen C, et al. Initial assessment of 3D magnetic resonance fingerprinting (MRF) towards quantitative brain imaging for radiation therapy. *Med Phys.* 2020;47(3):1199-1214.
239. Badve C, Yu A, Dastmalchian S, et al. MR Fingerprinting of Adult Brain Tumors: Initial Experience. *AJNR American journal of neuroradiology.* 2017;38(3):492-499.
240. Li T, Cui D, Hui ES, Cai J. Time-resolved magnetic resonance fingerprinting for radiotherapy motion management. *Med Phys.* 2020. doi: 10.1002/mp.14513.
241. Tian L, Di C, Ge R, Edward SH, Jing C. Investigation of the effect of acquisition schemes on time-resolved magnetic resonance fingerprinting. *Physics in Medicine & Biology.* 2021.
242. Heule R, Bause J, Pusterla O, Scheffler K. Multi-parametric artificial neural network fitting of phase-cycled balanced steady-state free precession data. *Magnetic Resonance in Medicine.* 2020;84(6):2981-2993.

243. Shcherbakova Y, van den Berg CAT, Moonen CTW, Bartels LW. PLANET: An ellipse fitting approach for simultaneous T1 and T2 mapping using phase-cycled balanced steady-state free precession. *Magn Reson Med.* 2018;79(2):711-722.
244. Heule R, Ganter C, Bieri O. Triple echo steady-state (TESS) relaxometry. *Magnetic Resonance in Medicine.* 2014;71(1):230-237.
245. Nguyen D, Bieri O. Motion-insensitive rapid configuration relaxometry. *Magn Reson Med.* 2017;78(2):518-526.
246. Juras V, Bohndorf K, Heule R, et al. A comparison of multi-echo spin-echo and triple-echo steady-state T2 mapping for in vivo evaluation of articular cartilage. *Eur Radiol.* 2016;26(6):1905-1912.
247. Kraff O, Lazik-Palm A, Heule R, Theysohn JM, Bieri O, Quick HH. 7 Tesla quantitative hip MRI: a comparison between TESS and CPMG for T2 mapping. *MAGMA.* 2016;29(3):503-512.
248. Riegler G, Drlicek G, Kronnerwetter C, et al. High-Resolution Axonal Bundle (Fascicle) Assessment and Triple-Echo Steady-State T2 Mapping of the Median Nerve at 7 T: Preliminary Experience. *Invest Radiol.* 2016;51(8):529-535.
249. Chen Y, Liu S, Wang Y, Kang Y, Haacke EM. STrategically Acquired Gradient Echo (STAGE) imaging, part I: Creating enhanced T1 contrast and standardized susceptibility weighted imaging and quantitative susceptibility mapping. *Magn Reson Imaging.* 2018;46:130-139.
250. Wang Y, Chen Y, Wu D, et al. STrategically Acquired Gradient Echo (STAGE) imaging, part II: Correcting for RF inhomogeneities in estimating T1 and proton density. *Magn Reson Imaging.* 2018;46:140-150.
251. Haacke EM, Chen Y, Utriainen D, et al. STrategically Acquired Gradient Echo (STAGE) imaging, part III: Technical advances and clinical applications of a rapid multi-contrast multi-parametric brain imaging method. *Magn Reson Imaging.* 2019;65:15-26.
252. Zhou J, Payen JF, Wilson DA, Traystman RJ, van Zijl PC. Using the amide proton signals of intracellular proteins and peptides to detect pH effects in MRI. *Nature medicine.* 2003;9(8):1085-1090.
253. Zhou J, Heo H-Y, Knutsson L, van Zijl PCM, Jiang S. APT-weighted MRI: Techniques, current neuro applications, and challenging issues. *Journal of magnetic resonance imaging : JMRI.* 2019;50(2):347-364.
254. Law BKH, King AD, Ai QY, et al. Head and Neck Tumors: Amide Proton Transfer MRI. *Radiology.* 2018;288(3):782-790.
255. Qamar S, King AD, Ai QY, et al. Amide proton transfer MRI detects early changes in nasopharyngeal carcinoma: providing a potential imaging marker for treatment response. *Eur Arch Otorhinolaryngol.* 2019;276(2):505-512.
256. Lee CY, Soliman H, Bragagnolo ND, et al. Predicting response to radiotherapy of intracranial metastases with hyperpolarized [Formula: see text]C MRI. *J Neurooncol.* 2021;152(3):551-557.
257. Cai J, Sheng K, Benedict SH, et al. Dynamic Mri of Grid-Tagged Hyperpolarized Helium-3 for the Assessment of Lung Motion during Breathing. *Int J Radiat Oncol.* 2009;75(1):276-284.
258. Kipritidis J, Tahir BA, Cazoulat G, et al. The VAMPIRE challenge: A multi-institutional validation study of CT ventilation imaging. *Med Phys.* 2019;46(3):1198-1217.

259. Cai J, Altes TA, Miller GW, et al. MR grid-tagging using hyperpolarized helium-3 for regional quantitative assessment of pulmonary biomechanics and ventilation. *Magnetic Resonance in Medicine.* 2007;58(2):373-380.
260. Ireland RH, Tahir BA, Wild JM, Lee CE, Hatton MQ. Functional Image-guided Radiotherapy Planning for Normal Lung Avoidance. *Clin Oncol (R Coll Radiol).* 2016;28(11):695-707.
261. Ye J, Bhagat SK, Li H, et al. Differentiation between recurrent gliomas and radiation necrosis using arterial spin labeling perfusion imaging. *Exp Ther Med.* 2016;11(6):2432-2436.
262. Eo T, Jun Y, Kim T, Jang J, Lee HJ, Hwang D. KIKI-net: cross-domain convolutional neural networks for reconstructing undersampled magnetic resonance images. *Magnetic resonance in medicine : official journal of the Society of Magnetic Resonance in Medicine / Society of Magnetic Resonance in Medicine.* 2018;80(5):2188-2201.
263. Schlemper J, Caballero J, Hajnal JV, Price AN, Rueckert D. A Deep Cascade of Convolutional Neural Networks for Dynamic MR Image Reconstruction. *IEEE Trans Med Imaging.* 2018;37(2):491-503.
264. Souza R, Frayne R. A Hybrid Frequency-Domain/Image-Domain Deep Network for Magnetic Resonance Image Reconstruction. Paper presented at: 2019 32nd SIBGRAPI Conference on Graphics, Patterns and Images (SIBGRAPI); 28-30 Oct. 2019, 2019.
265. Yang G, Yu S, Dong H, et al. DAGAN: Deep De-Aliasing Generative Adversarial Networks for Fast Compressed Sensing MRI Reconstruction. *IEEE Trans Med Imaging.* 2018;37(6):1310-1321.
266. Virtue P, Yu SX, Lustig M. Better than real: Complex-valued neural nets for MRI fingerprinting. Paper presented at: 2017 IEEE International Conference on Image Processing (ICIP); 17-20 Sept. 2017, 2017.
267. Boulanger M, Nunes JC, Chourak H, et al. Deep learning methods to generate synthetic CT from MRI in radiotherapy: A literature review. *Phys Med.* 2021;89:265-281.
268. Koike Y, Akino Y, Sumida I, et al. Feasibility of synthetic computed tomography generated with an adversarial network for multi-sequence magnetic resonance-based brain radiotherapy. *J Radiat Res.* 2020;61(1):92-103.
269. Olberg S, Chun J, Su Choi B, et al. Abdominal synthetic CT reconstruction with intensity projection prior for MRI-only adaptive radiotherapy. *Physics in medicine and biology.* 2021;66(20).
270. Morbée L, Chen M, Herregods N, Pullens P, Jans LBO. MRI-based synthetic CT of the lumbar spine: Geometric measurements for surgery planning in comparison with CT. *Eur J Radiol.* 2021;144:109999.
271. Tie X, Lam SK, Zhang Y, Lee KH, Au KH, Cai J. Pseudo-CT generation from multi-parametric MRI using a novel multi-channel multi-path conditional generative adversarial network for nasopharyngeal carcinoma patients. *Med Phys.* 2020;47(4):1750-1762.
272. Kleesiek J, Morshuis JN, Isensee F, et al. Can virtual contrast enhancement in brain MRI replace gadolinium?: a feasibility study. 2019;54(10):653-660.
273. Gong E, Pauly JM, Wintermark M, Zaharchuk GJJomri. Deep learning enables reduced gadolinium dose for contrast-enhanced brain MRI. 2018;48(2):330-340.
274. Zhou T, Fu H, Chen G, Shen J, Shao LJItomi. Hi-net: hybrid-fusion network for multi-modal MR image synthesis. 2020.

275. Li W, Li Y, Qin W, et al. Magnetic resonance image (MRI) synthesis from brain computed tomography (CT) images based on deep learning methods for magnetic resonance (MR)-guided radiotherapy. 2020;10(6):1223.
276. Xu C, Zhang D, Chong J, Chen B, Li S. Synthesis of gadolinium-enhanced liver tumors on nonenhanced liver MR images using pixel-level graph reinforcement learning. *Med Image Anal.* 2021;69:101976.
277. Yu B, Zhou L, Wang L, Fripp J, Bourgeat P. 3D cGAN based cross-modality MR image synthesis for brain tumor segmentation. Paper presented at: 2018 IEEE 15th International Symposium on Biomedical Imaging (ISBI 2018)2018.
278. Li W, Xiao H, Li T, et al. Virtual Contrast-enhanced Magnetic Resonance Images Synthesis for Patients With Nasopharyngeal Carcinoma Using Multimodality-guided Synergistic Neural Network. *Int J Radiat Oncol Biol Phys.* 2021. doi: 10.1016/j.ijrobp.2021.11.007.